

Generative Modelling of Structurally Constrained Graphs

Manuel Madeira

EPFL, Lausanne, Switzerland
manuel.madeira@epfl.ch

Clément Vignac

EPFL, Lausanne, Switzerland

Dorina Thanou

EPFL, Lausanne, Switzerland

Pascal Frossard

EPFL, Lausanne, Switzerland

Abstract

Graph diffusion models have emerged as state-of-the-art techniques in graph generation, yet integrating domain knowledge into these models remains challenging. Domain knowledge is particularly important in real-world scenarios, where invalid generated graphs hinder deployment in practical applications. Unconstrained and conditioned graph generative models fail to guarantee such domain-specific structural properties. We present ConStruct, a novel framework that allows for hard-constraining graph diffusion models to incorporate specific properties, such as planarity or acyclicity. Our approach ensures that the sampled graphs remain within the domain of graphs that verify the specified property throughout the entire trajectory in both the forward and reverse processes. This is achieved by introducing a specific edge-absorbing noise model and a new projector operator. ConStruct demonstrates versatility across several structural and edge-deletion invariant constraints and achieves state-of-the-art performance for both synthetic benchmarks and attributed real-world datasets. For example, by leveraging planarity in digital pathology graph datasets, the proposed method outperforms existing baselines and enhances generated data validity by up to 71.1 percentage points.

1 Introduction

Learning how to generate realistic graphs that faithfully mirror a target distribution is crucial for tasks such as data augmentation in network analysis or discovery of novel network structures. This has become a prominent problem in diverse real-world modelling scenarios, ranging from molecule design [54] and inverse protein folding [84] to anti-money laundering [44] or combinatorial optimization [74]. While the explicit representation of relational and structural information with graphs encourage their widespread adoption in numerous applications, their sparse and unordered nature make the task of graph generation challenging.

In many real-world problems, we possess a priori knowledge about specific properties of the target distribution of graphs. Incorporating such knowledge into generative models is a natural approach to enforce the generated graphs to comply with the domain-specific properties. Indeed, common generative models, even when conditioned towards graph desired properties, fail to offer guarantees. This may however become particularly critical in settings where noncompliant graphs can lead to real-world application failures. Many of these desired properties are edge-related, i.e., constraints in the structure of the graph. For example, in digital pathology, graphs extracted from tissue slides are planar [25, 67]. Similarly, in contact networks between patients and healthcare workers within hospitals, the degrees of healthcare workers are upper bounded to effectively prevent the emergence of superspreaders and mitigate the risk of infectious disease outbreaks [31, 1]. In graph generation,

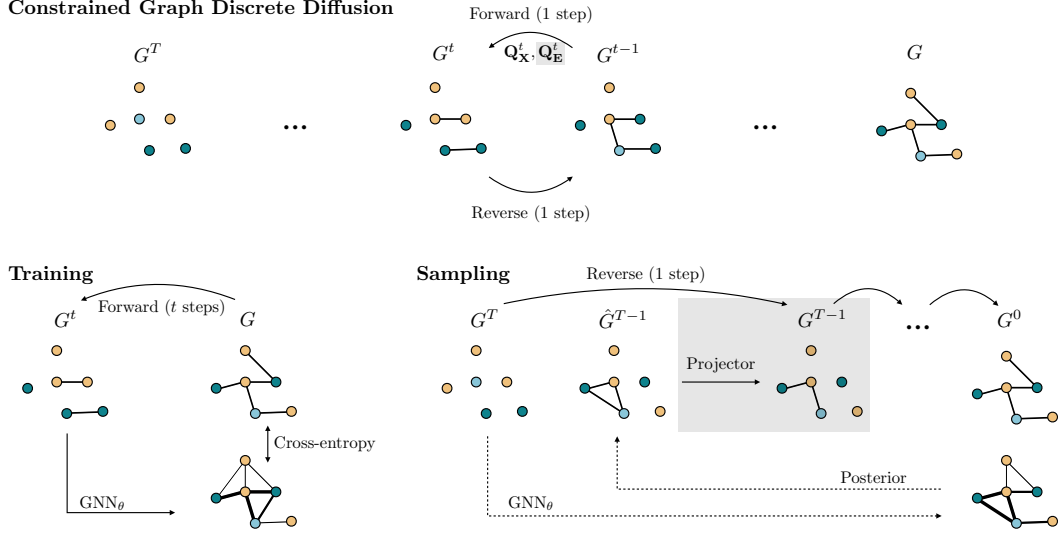


Figure 1: Constrained graph discrete diffusion framework. The forward process consists of an edge deletion process driven by the edge-absorbing noise model, while the node types may switch according to the marginal noise model. The projector operator ensures that sampled graphs remain within the constrained domain throughout the entire reverse process. In this case, the constrained domain consists exclusively of graphs with no cycles. We highlight in gray the components responsible for preserving the constraining property.

diffusion models have led to state-of-the-art performance [77, 63, 6], in line with their success on other data modalities [73, 28]. However, constrained generation still lags behind its unconstrained counterpart: despite the remarkable expressivity of graph diffusion models, constraining them to leverage specific graph properties remains a particularly challenging task [40].

In this paper, we propose ConStruct, a constrained graph discrete diffusion framework that induces specific structural properties in generative models. Our focus lies on a broad family of structural properties that hold upon edge deletion, including graph planarity or absence of cycles or triangles, for example. ConStruct operates within graph discrete diffusion, where both node and edge types lie in discrete state-spaces [77, 26, 63, 9]. Notably, ConStruct is designed to preserve both the forward and reverse processes of the diffusion model within distribution with respect to a specified structural property. To accomplish this, we introduce two main components: an edge absorbing noise model and an efficient projector of the target property. The former casts the forward process as an edge deletion process and the reverse process as an edge insertion process. Simultaneously, the projector ensures that the inserted edges in the reverse process, predicted by a trained graph neural network, do not violate the structural property constraints. We theoretically ground the projector design by proving that it can retrieve the optimal graph under a graph edit distance setting. Additionally, we further enhance its efficiency by leveraging incremental constraint satisfaction algorithms, as opposed to their full graph versions, and a blocking edge hash table to avoid duplicate constraint property satisfaction checks. These two components enable a reduction in computational redundancy throughout the reverse process.

We empirically validate the benefit of promoting the match of distributions between the training and generative processes in terms of sample quality and constraint satisfaction on a set of benchmark datasets, outperforming unconstrained methods. We demonstrate the flexibility of ConStruct by testing it with three distinct structural properties constraints: graph planarity, acyclicity and lobster components. To further illustrate the utility of ConStruct to real-world applications, we evaluate the performance of our model in generating biologically meaningful cell-cell interactions, represented through planar cell graphs derived from digital pathology data. We focus on the generation of simple yet medically significant tertiary lymphoid structures [43, 17, 57, 27, 67]. Our experiments demonstrate a significant improvement in cell graph generation with ConStruct compared to unconstrained methods [51], notably achieving an increase of up to 71.1 percentage points in terms of cell graph va-

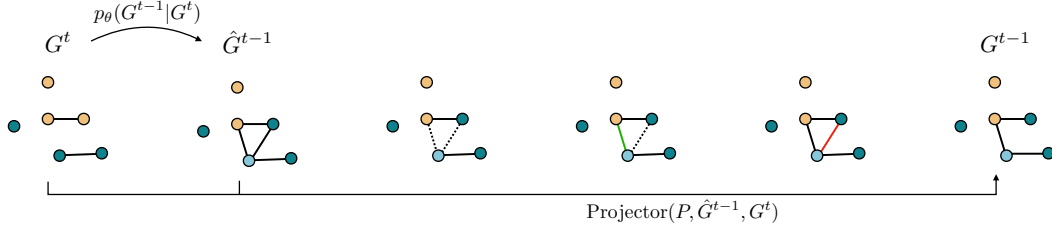


Figure 2: Projector operator. At each iteration, we start by sampling a candidate graph \hat{G}^{t-1} from the distribution $p_\theta(G^{t-1}|G^t)$ provided by the diffusion model. Then, the projector step inserts in an uniformly random manner the candidate edges, discarding those that violate the target property, P , i.e., acyclicity in this illustration. In the end of the reverse step, we find a graph G^{t-1} that is guaranteed to comply with such property.

lidity. These results open new venues for innovative data augmentation techniques and novel instance discovery, addressing a key challenge in digital pathology and real-world applications in general. ¹

2 Related Work

By decomposing the graph generation task into multiple denoising steps, graph diffusion models have gained prominence due to their superior generative performance among methods that predict the full adjacency matrix at once (e.g., VAEs [39, 72, 76, 36], GANs [15, 41, 53], and normalizing flows [47, 52, 46, 50]). Diverse diffusion formulations have emerged to address different particularities of the graph setting, encompassing score-based approaches [59, 37, 83] and discrete diffusion [77, 26, 63]. They have also been used in intermediate steps for specific generation schemes, such as iterative local expansion [6]. Graph diffusion models are amenable to conditional graph generation techniques, which, despite enabling the guidance of the generation process towards graphs with desired properties, do not guarantee the satisfaction of such properties [77, 30]. Additionally, graph diffusion models can leverage formulations that are invariant to permutations, avoiding the sensitivity to node ordering that characterizes autoregressive models [85, 45, 13]. However, while the latter can straightforwardly ensure constraint satisfaction through validity checks at each iteration, the former still lag behind in addressing this challenge.

Previous approaches to close such gap can be categorized according to the assumed nature of graph state-spaces. In the continuous case, PRODIGY [70] exploits the projection of the sampled graph onto the constraint satisfying set at each reverse step. It can impose simple structural and molecular properties for which a closed-form projection can be derived. While this approach has shown success in other data modalities [11], applying a continuous state-space projection on the adjacency matrix and categorical node features can pervert their inherent discreteness and compromise the smoothness of the denoising process. Additionally, such an operator can not be derived to combinatorial constraints over the graph structure, as is often encountered in real-world scenarios (e.g., planarity or acyclicity).

Then, in discrete state-spaces, EDGE [9] leverages a node-wise maximum degree hard constraint due to its degree guidance but it is limited to this particular property. Similarly, GraphARM [40], a graph autoregressive diffusion model, allows for constraint incorporation in the autoregressive manner. However, this method requires learning a node ordering, a task at least as complex as isomorphism testing. Therefore, to the best of our knowledge, ConStruct consists of the first graph constrained discrete diffusion framework covering a broad class of structural (potentially combinatorial) constraints.

3 Constrained Graph Diffusion Models

We now introduce our framework on generative modelling for structurally constrained graphs. We first present the graph diffusion framework and then focus on the new components for constrained graph generation.

¹Our code and data are available at <https://github.com/manuelfmadeira/ConStruct>.

3.1 Graph Diffusion Models

We first introduce the notation used in our model:

Notation We define a graph as $G = (X, E)$, where X and E denote the sets of attributed nodes and edges, respectively. We consider the node and edge features to be categorical and to lie in the spaces \mathcal{X} and \mathcal{E} of cardinalities b and c , respectively. Thus, x_i denotes the node attribute of node i and e_{ij} the edge attribute of the edge between nodes i and j . With $\mathcal{H}^k = \{\mathbf{v} = (v_1, \dots, v_k) \mid v_i \in \{0, 1\}, \sum_{i=1}^k v_i = 1\}$, their corresponding one-hot encodings are then $\mathbf{x}_i \in \mathcal{H}^b$ and $\mathbf{e}_{ij} \in \mathcal{H}^{c+1}$, since we consider the absence of edge between two nodes as an edge type (“no edge” type). These are stacked in tensors $\mathbf{X} \in \{0, 1\}^{n \times b}$ and $\mathbf{E} \in \{0, 1\}^{n \times n \times (c+1)}$, respectively. So, equivalently to the set notation, we also have $G = (\mathbf{X}, \mathbf{E})$.

We then recall the core components of generative models based on graph diffusion, a state-of-the-art framework in several applications [37, 77]. Graph diffusion models are composed of two main processes: a *forward* and a *reverse* one. The forward process consists of a Markovian noise model, q , with T timesteps, that allows to progressively perturb a clean graph G to its noisy version G^t , where $t \in \{1, \dots, T\}$. This process is typically modelled independently for nodes and edges. The reverse process consists of the opposite development, starting from a fully noisy, G^T , and iteratively refining it until a new clean sample is generated. This process uses a denoising neural network (NN), the only learnable part of the diffusion model. The NN is trained to predict a probability distribution over node and edge types of the clean graph G . After its training, we combine the NN prediction with the posterior term of the forward process to find the distribution $p_\theta(G^{t-1}|G^t)$, from where we sample a one-step denoised graph. The reverse process results from applying this sampling procedure iteratively until we arrive to a fresh new clean graph G^0 . Both processes are illustrated in Figure 1.

In some tasks, we are interested in only generating instances of a specific class of graphs that match the training distribution together with specific structural properties. This becomes particularly crucial, for instance, in scenarios where we possess domain knowledge but lack sufficient data for an unconstrained model to capture strict dependencies. It also applies to many real-world applications, where graphs that do not respect certain conditions are not feasible or have no physical meaning (e.g., drug design). Despite the remarkable expressivity of graph diffusion models, incorporating such constraints into their generative process remains a largely unsolved problem.

3.2 Constrained Graph Discrete Diffusion Models

We now introduce ConStruct, a framework that efficiently constrains graph diffusion models based on structural properties. Constraining graph generation implies guaranteeing that such target structural properties are not violated in the generated graphs. We build on graph discrete diffusion due to its intrinsic capability to effectively preserve fundamental structural properties (e.g., sparsity) of graphs throughout the generative process [77, 26].

A successful way of imposing constraints to diffusion models in continuous state-spaces consists of constraining the domain where the forward and reverse processes occur [49, 21, 22]. However, constraining domains over graphs, which are inherently discrete, poses a challenging combinatorial problem. Instead, we propose to constrain the graph generative process with specific structural properties. In our approach, we explore the broad class of graph structural properties that hold under edge deletion, namely *edge-deletion invariant* properties.

Definition 3.1. (Edge-Deletion Invariance) *Let P be a boolean-valued application defined on graphs, referred to as a property. P is said to be edge-deletion invariant if, for any graph G and any subset of edges $\tilde{E} \subset E$, it satisfies:*

$$P(G) = \text{True} \implies P(G') = \text{True}, \quad \text{with } G' = (X, E \setminus \tilde{E}).$$

Many properties that are observed in real-world scenarios are edge-deletion invariant. For example, graph planarity is observed in road networks [81], chip design [7], biochemistry [71] or digital pathology [34]. In evolutionary biology [24] or epidemiology [68], we find graphs that must not have cycles. Also, maximum degree constraints are quite common in the design of contact networks [31, 1]. Finally, Definition 3.1 is extendable to continuous graph-level features through a binary decision (e.g., by thresholding continuous values into a boolean value).

Provided that the training graphs satisfy the target structural properties, ConStruct enforces these properties in the generated graphs by relying on two main components: an edge-absorbing noise model and a projector. These two components are described in detail below.

3.3 Edge-deletion Aware Forward Process

Our goal is to design a forward process that yields noisy graphs that necessarily satisfy the target property. This process is typically modelled using transition matrices. Thus, $[\mathbf{Q}_X^t]_{ij} = q(x^t = j | x^{t-1} = i)$ corresponds to the probability of a node transitioning from type i to type j . Similarly, for edges we have $[\mathbf{Q}_E^t]_{ij} = q(e^t = j | e^{t-1} = i)$. These are applied independently to each node and edge, yielding $q(G^t | G^{t-1}) = (\mathbf{X}^{t-1} \mathbf{Q}_X^t, \mathbf{E}^{t-1} \mathbf{Q}_E^t)$. Consequently, we can directly jump t timesteps in the forward step through the categorical distribution given by:

$$q(G^t | G) = (\mathbf{X} \bar{\mathbf{Q}}_X^t, \mathbf{E} \bar{\mathbf{Q}}_E^t), \quad (1)$$

with $\bar{\mathbf{Q}}_X^t = \mathbf{Q}_X^1 \dots \mathbf{Q}_X^t$ and $\bar{\mathbf{Q}}_E^t = \mathbf{Q}_E^1 \dots \mathbf{Q}_E^t$. Noising a graph amounts to sampling a graph from this distribution. For the nodes, we use the marginal noise model [77] due to its great empirical performance. Importantly, to preserve the constraining structural property throughout the forward process, and, consequently, throughout the training algorithm (see Algorithm 1 in Appendix), we propose the utilization of an *edge-absorbing noise model* [3]. This noise model forces each edge to either remain in the same state or to transition to an absorbing state (which we define to be the no-edge state) throughout the forward process. This edge noise model poses the forward as an edge deletion process, converging to a limit distribution that yields graphs without edges. Therefore, we obtain the following transition matrices:

$$\begin{aligned} \mathbf{Q}_X^t &= \alpha^t \mathbf{I} + (1 - \alpha^t) \mathbf{1}_b \mathbf{m}'_X \quad \text{and} \\ \mathbf{Q}_E^t &= \alpha_{\text{ABS}}^t \mathbf{I} + (1 - \alpha_{\text{ABS}}^t) \mathbf{1}_c \mathbf{e}'_E, \end{aligned} \quad (2)$$

where α^t and α_{ABS}^t transition from 1 to 0 with t according to the popular cosine scheduling [58] and the mutual-information-based noise schedule ($\alpha^t = 1 - (T + t + 1)^{-1}$) [3], respectively. The vectors $\mathbf{1}_b \in \{1\}^b$ and $\mathbf{1}_c \in \{1\}^{c+1}$ are filled with ones, and $\mathbf{m}'_X \in \Delta^b$ and $\mathbf{e}'_E \in \{0, 1\}^{c+1}$ are row vectors filled with the marginal node distribution and the one-hot encoding of the no-edge state, respectively.

3.4 Structurally-Constrained Reverse Process

The reverse process of the diffusion model is fully characterized by the distribution $p_\theta(G^{t-1} | G^t)$. We detail how to build it from the predictions of a denoising graph neural network, (GNN_θ) , and the posterior term of the forward process in Appendix A.1. Importantly, the latter imposes the reverse process as an edge insertion process, yet does not necessarily ensure the target structural property. To handle that, we propose an intermediate procedure for each reverse step. Provided a noisy graph G^t at timestep t , we do not accept directly \hat{G}^{t-1} , sampled from $p_\theta(G^{t-1} | G^t)$, as the one step denoised graph. Instead, we iteratively add the newly added edges to \hat{G}^{t-1} in a random order, discarding the ones that lead to the violation of the target property. Therefore, we only have $G^{t-1} = \hat{G}^{t-1}$ if none of the candidate edges breaks the target property. We refer to the operator that outputs G^{t-1} provided \hat{G}^{t-1} and G^t by discarding the violating edges as the *projector*. Its implementation is illustrated in Figure 2 and described in Algorithm 3 in Appendix. Importantly, this procedure merely interferes with the sampling algorithm (refer to Algorithm 2 in Appendix) and ensures that the diffusion model training remains unaffected, preserving its efficiency.

Despite its algorithmic simplicity, the design of our projector is theoretically motivated by the result below. We denote the graph edit distance [66] with uniform cost between two graphs G_1 and G_2 by $\text{GED}(G_1, G_2)$ (see Definition B.1).

Theorem 1. (Simplified) *Let $\mathcal{G}^{t-1} = \text{Projector}(P, \hat{G}^{t-1}, G^t)$ be the set of all possible one-step denoised graphs outputted by ConStruct. If we define G^* as any optimal solution of:*

$$\min_{G \in \mathcal{C}} \text{GED}(\hat{G}^{t-1}, G), \quad (3)$$

where $\mathcal{C} = \{G \in \mathcal{G} | P(G) = \text{True}, G \supset G^t\}$, with \mathcal{G} the set of all unattributed graphs, then G^ can be recovered by our projector, i.e., $G^* \in \mathcal{G}^{t-1}$.*

The relationship between the projector and the candidate element \hat{G}^{t-1} (the instance we aim to project onto a constrained set) and the specified target property P (defining the constrained set) can be analogized to the conventional projection operator in continuous state spaces. However, while projection in continuous spaces is typically straightforward, this is not the case for discrete state spaces, where, for instance, there often lacks an inherent notion of order between different states. In particular, projecting into an arbitrary subclass of graphs is a complex general combinatorial problem to which there is no efficient solution. For example, finding the maximum planar subgraph of a given graph is NP-hard [10]. Therefore, the novelty of our method is introduced by considering an additional dependency on G^t : to make such problem efficiently approachable, we use the previous iterate, G^t , which we know by construction that verifies the target property, as a reference. This information is added into the optimization problem through the formulation of the set C . Importantly, this formulation is consistent with the designed noise for the diffusion model, as it complies with the reverse process as an edge insertion process (i.e., $G^t \subset G^{t-1}$). The complete version of this theorem and extensions for specific constraints can be found in Appendix B.

Importantly, the utilization of the projector breaks the independent sampling of new edges since the insertion of an edge now depends on the order by which we insert them at a given timestep. This sacrifices the tractability of an evidence lower bound for the diffusion model’s likelihood. In exchange, it conserves all the sampled graphs throughout the reverse process in the constrained domain. Therefore, the edge-absorbing noise model and the projector jointly ensure that the graph distributions of the training and sampling procedures match, within the predefined constrained graph domain. With these blocks in place, we are now able to both train and sample from the constrained diffusion model.

3.5 Implementation Improvements

We further enhance the efficiency of the sampling algorithm with the two improvements detailed below.

Blocking Edge Hash Table Throughout the reverse process, we keep in memory the edges that have already been rejected in previous timesteps (higher t). Therefore, once an edge is rejected, it is blocked throughout the rest of the reverse process. This prevents the repetition of redundant constraint satisfaction checks since we know *a priori* that inserting a previously rejected edge would lead to constraint violation. We store this information in a hash table, where both the lookup and update operations are $O(1)$, causing minor overhead. Since we only perform the validity check, of complexity $O(V)$, once for each edge - if it is a candidate edge, we either insert it or block it -, it incurs a $O(n^2V)$ overhead throughout the full reverse process. Note that we lose any dependency on the number of timesteps of the reverse process, which is typically the limiting factor in diffusion models efficiency due to its required high values ($T \approx 10^3$).

Incremental Algorithms Our reverse process consists solely of edge insertion steps, making it well-suited for the application of incremental algorithms. These algorithms efficiently check whether newly added edges preserve the target property by updating and checking smartly designed representations of the graph. This approach contrasts with full graph counterparts, leading to significant efficiency gains by reducing redundant computation. For instance, while the best full planar testing algorithm is $O(n)$ [29], its fastest known incremental test has amortized running time of $O(\alpha(q, n))$, where q is the total number of operations (edge queries and insertions), and α denotes the inverse-Ackermann function [42] (often considered “almost constant” complexity). More details for different properties in Appendix C.

In practice, we observe the projector to incur a minor overhead in the runtime of the diffusion model sampling when compared to the model’s quadratic dependency on edge prediction for every timestep (see Appendix D.3).

4 Experiments

In this section, we first explore the flexibility of ConStruct to accommodate different constraints in synthetic unattributed graph datasets. Then, we test its applicability to a real-world scenario with digital pathology data.

Table 1: Graph generation performance on synthetic graphs. We present the results over five sampling runs of 100 generated graphs each, in the format mean \pm standard error of the mean. The remaining values are retrieved from Bergmeister et al. [6] for the planar and tree datasets, and from Dai et al. [13] and Jang et al. [33] for the lobster dataset. For the average ratio computation, we follow [6] and do not consider the metrics whose train set MMD is 0. We recompute the train set MMDs according to our splits but, for fairness, in the retrieved methods the average ratio metric is not recomputed.

Planar Dataset											
Model	Deg. \downarrow	Clus. \downarrow	Orbit \downarrow	Spec. \downarrow	Wavelet \downarrow	Ratio \downarrow	Valid \uparrow	Unique \uparrow	Novel \uparrow	V.U.N. \uparrow	Property \uparrow
Train set	0.0002	0.0310	0.0005	0.0038	0.0012	1.0	100	100	0.0	0.0	100
GraphRNN [85]	0.0049	0.2779	1.2543	0.0459	0.1034	490.2	0.0	100	100	0.0	—
GRAN [45]	0.0007	0.0426	0.0009	0.0075	0.0019	2.0	97.5	85.0	2.5	0.0	—
SPECTRE [53]	0.0005	0.0785	0.0012	0.0112	0.0059	3.0	25.0	100	100	25.0	—
DiGress [77]	0.0007	0.0780	0.0079	0.0098	0.0031	5.1	77.5	100	100	77.5	—
EDGE [9]	0.0761	0.3229	0.7737	0.0957	0.3627	431.4	0.0	100	100	0.0	—
BwR [16]	0.0231	0.2596	0.5473	0.0444	0.1314	251.9	0.0	100	100	0.0	—
BiGG [13]	0.0007	0.0570	0.0367	0.0105	0.0052	16.0	62.5	85.0	42.5	5.0	—
GraphGen [23]	0.0328	0.2106	0.4236	0.0430	0.0989	210.3	7.5	100	100	7.5	—
HSpectre (one-shot) [6]	0.0003	0.0245	0.0006	0.0104	0.0030	1.7	67.5	100	100	67.5	—
HSpectre [6]	0.0005	0.0626	0.0017	0.0075	0.0013	2.1	95.0	100	100	95.0	—
DiGress+	0.0008 \pm 0.0001	0.0410 \pm 0.0033	0.0048 \pm 0.0004	0.0056 \pm 0.0004	0.0020 \pm 0.0002	3.6 \pm 0.2	76.4 \pm 1.3	100.0 \pm 0.0	100.0 \pm 0.0	76.4 \pm 1.3	76.4 \pm 1.3
ConStruct	0.0003 \pm 0.0001	0.0403 \pm 0.0047	0.0004 \pm 0.0001	0.0053 \pm 0.0004	0.0009 \pm 0.0001	1.1 \pm 0.1	100.0 \pm 0.0	100.0 \pm 0.0	100.0 \pm 0.0	100.0 \pm 0.0	100.0 \pm 0.0
Tree Dataset											
Train set	0.0001	0.0000	0.0000	0.0075	0.0030	1.0	100	100	0.0	0.0	100
GRAN [45]	0.1884	0.0080	0.0199	0.2751	0.3274	607.0	0.0	100	100	0.0	—
DiGress [77]	0.0002	0.0000	0.0000	0.0113	0.0043	1.6	90.0	100	100	90.0	—
EDGE [9]	0.2678	0.0000	0.7357	0.2247	0.4230	850.7	0.0	7.5	100	0.0	—
BwR [16]	0.0016	0.1239	0.0003	0.0480	0.0388	11.4	0.0	100	100	0.0	—
BiGG [13]	0.0014	0.0000	0.0000	0.0119	0.0058	5.2	100	87.5	50.0	75.0	—
GraphGen [23]	0.0105	0.0000	0.0000	0.0153	0.0122	33.2	95.0	100	100	95.0	—
HSpectre (one-shot) [6]	0.0004	0.0000	0.0000	0.0080	0.0055	2.1	82.5	100	100	82.5	—
HSpectre [6]	0.0001	0.0000	0.0000	0.0117	0.0047	4.0	100	100	100	100	—
DiGress+	0.0002 \pm 0.0001	0.0000 \pm 0.0000	0.0000 \pm 0.0000	0.0092 \pm 0.0005	0.0032 \pm 0.0001	1.3 \pm 0.2	91.6 \pm 0.7	100.0 \pm 0.0	100.0 \pm 0.0	91.6 \pm 0.7	97.0 \pm 0.8
ConStruct	0.0003 \pm 0.0001	0.0000 \pm 0.0000	0.0000 \pm 0.0000	0.0073 \pm 0.0008	0.0034 \pm 0.0002	1.9 \pm 0.3	83.0 \pm 1.8	100.0 \pm 0.0	100.0 \pm 0.0	83.0 \pm 1.8	100.0 \pm 0.0
Lobster Dataset											
Train set	0.0002	0.0000	0.0000	0.0070	0.0070	1.0	100	100	0.0	0.0	100
GraphRNN [85]	0.000	0.000	0.000	0.011	—	—	100	—	—	—	—
GRAN [45]	0.038	0.000	0.001	0.027	—	—	88.0	—	—	—	—
GraphGen [23]	0.548	0.040	0.247	—	—	—	—	—	—	—	—
GraphGen-Redux [4]	1.189	1.859	0.885	—	—	—	—	—	—	—	—
BiGG [13]	0.000	0.000	0.000	0.009	—	—	100	—	—	—	—
GDSS [37]	0.117	0.002	0.149	—	—	—	18.2	100	100	18.2	—
BwR [16]	0.316	0.000	0.247	—	—	—	100	63.6	100	63.6	—
GEEL [33]	0.002	0.000	0.001	—	—	—	72.7	100	72.7	\leq 72.7	—
HGGT [32]	0.003	0.000	0.015	—	—	—	—	—	—	—	—
DiGress [77]	0.021	0.000	0.004	—	—	—	54.5	100	100	54.5	—
DiGress+	0.0005 \pm 0.0001	0.0000 \pm 0.0000	0.0000 \pm 0.0000	0.0114 \pm 0.0006	0.0093 \pm 0.0005	1.8 \pm 0.1	79.0 \pm 1.1	98.0 \pm 0.7	96.6 \pm 0.6	69.4 \pm 1.2	76.8 \pm 1.7
ConStruct	0.0003 \pm 0.0001	0.0000 \pm 0.0000	0.0000 \pm 0.0000	0.0092 \pm 0.0009	0.0074 \pm 0.0004	1.3 \pm 0.2	86.8 \pm 2.4	98.8 \pm 0.6	97.0 \pm 0.9	83.2 \pm 2.3	100.0 \pm 0.0

4.1 Synthetic Graphs

Setup We focus on three synthetic datasets with different structural properties: the *planar* dataset [53], composed of planar and connected graphs; the *tree* dataset [6], composed of connected graphs without cycles (tree graph); and the *lobster* dataset [45], composed of connected graphs without cycles, where no node is more than 2 hops away from a backbone path (lobster graph). We follow the splits originally proposed for each of the datasets: 80% of the graphs are used in the training set and the remaining 20% are allocated to the test set. We use 20% of the train set as validation set. Statistics of these datasets are shown in Appendix E. As the graphs in these datasets are unattributed, we can specifically isolate ConStruct’s capability of incorporating structural information in comparison to previously proposed methods, which are described in Appendix E.2. From here on, we use DiGress+ to denote the DiGress model with the added extra features described in Appendix A.1 and HSpectre to refer to the model proposed by Bergmeister et al. [6].

Regarding performance metrics, we follow the evaluation procedures from Martinkus et al. [53]. We assess how close the distributions of different graph statistics computed from the generated and test sets are. To accomplish that, we compute the Maximum Mean Discrepancy (MMD)² for the node degrees (Deg.), clustering coefficients (Clus.), orbit count (Orbit), eigenvalues of the normalized graph Laplacian (Spec.), and statistics from a wavelet graph transform (Wavelet). To summarize this set of metrics, we compute the ratio over the same metrics obtained by the train set and average it (Ratio). We also compute the proportion of non-isomorphic graphs (Unique), the proportion of graphs non-isomorphic to any graph in the train set (Novel) and the proportion of valid generated graphs (Valid). Graphs are considered valid if they are planar and connected, trees, or lobster graphs, when the generative model is trained on the planar, tree, or lobster dataset, respectively. We merge

²To align with previous literature, we actually compute MMD^2 .

Table 2: Graph generation performance on digital pathology graphs. We present the results for each method over five sampling runs of 100 generated graphs each, in the format mean \pm standard error of the mean.

Low TLS Dataset											
Model	Ratio ↓	Conn. ↑	Planar ↑	V.U.N. ↑	$\kappa(0)$ ↓	$\kappa(1)$ ↓	$\kappa(2)$ ↓	$\kappa(3)$ ↓	$\kappa(4)$ ↓	$\kappa(5)$ ↓	TLS Valid ↑
Train set	1.0	100	100	0.0	0.6928	0.0000	0.0000	0.0000	0.0000	0.0000	100
Baseline [51]	194.6 ±3.0	50.3 ±0.7	10.0 ±0.5	0.0 ±0.0	0.6256 ±0.0228	0.2350 ±0.0000	0.2350 ±0.0000	0.0470 ±0.0470	0.0000 ±0.0000	0.0000 ±0.0000	0.0 ±0.0
GraphGen [23]	212.7 ±4.2	100.0 ±0.0	33.3 ±0.5	33.0 ±1.8	0.7354 ±0.0220	0.1880 ±0.0470	0.0470 ±0.0470	0.0000 ±0.0000	0.0000 ±0.0000	0.0000 ±0.0000	33.3 ±0.5
BiGG [13]	132.0 ±6.3	99.5 ±0.1	23.3 ±0.6	0.8 ±0.2	0.6184 ±0.0437	0.1410 ±0.0576	0.0470 ±0.0470	0.0470 ±0.0470	0.0470 ±0.0470	0.0470 ±0.0470	23.3 ±0.6
SPECTRE [53]	427.0 ±4.3	95.3 ±0.2	51.2 ±0.6	15.8 ±1.2	0.2350 ±0.0000	0.0000 ±0.0000	0.0000 ±0.0000	0.0000 ±0.0000	0.0000 ±0.0000	0.0000 ±0.0000	50.6 ±0.7
DiGress+	4.9 ±1.0	96.0 ±0.7	19.8 ±1.8	18.6 ±1.8	0.7306 ±0.0371	0.1410 ±0.0576	0.0000 ±0.0000	0.0000 ±0.0000	0.0000 ±0.0000	0.0000 ±0.0000	18.6 ±1.8
ConStruct	4.4 ±0.3	98.4 ±0.8	100.0 ±0.0	98.4 ±0.8	0.6781 ±0.0795	0.2350 ±0.0000	0.0940 ±0.0576	0.0000 ±0.0000	0.0000 ±0.0000	0.0000 ±0.0000	96.2 ±0.7
High TLS Dataset											
Train set	1.0	100	100	0.0	0.4257	0.4512	0.4745	0.6395	0.7770	0.7663	100
Baseline [51]	354.9 ±2.2	49.8 ±0.3	3.4 ±0.2	0.2 ±0.2	0.3276 ±0.0023	0.3412 ±0.0070	0.3669 ±0.0172	0.5096 ±0.0157	0.6231 ±0.0176	0.6988 ±0.0203	0.0 ±0.0
GraphGen [23]	559.1 ±9.8	100.0 ±0.0	48.1 ±0.6	47.4 ±1.6	0.3311 ±0.0158	0.3620 ±0.0228	0.4613 ±0.0121	0.6034 ±0.0359	0.7500 ±0.0231	0.7523 ±0.0346	16.9 ±0.6
BiGG [13]	307.7 ±15.5	99.5 ±0.1	10.1 ±0.8	0.4 ±0.2	0.3706 ±0.0225	0.4850 ±0.0361	0.5970 ±0.0166	0.7151 ±0.0112	0.7494 ±0.0128	0.7515 ±0.0220	10.0 ±0.8
SPECTRE [53]	938.1 ±4.1	91.3 ±0.3	0.0 ±0.0	0.0 ±0.0	0.3190 ±0.0293	0.3585 ±0.0279	0.4033 ±0.0230	0.5130 ±0.0230	0.6039 ±0.0127	0.6804 ±0.0137	0.0 ±0.0
DiGress+	10.5 ±0.6	97.8 ±0.8	8.4 ±1.1	7.8 ±1.2	0.3194 ±0.0034	0.3308 ±0.0041	0.3598 ±0.0096	0.4878 ±0.0155	0.6234 ±0.0305	0.6887 ±0.0250	6.6 ±0.9
ConStruct	6.4 ±0.6	99.8 ±0.2	100.0 ±0.0	99.8 ±0.2	0.3378 ±0.0048	0.3437 ±0.0104	0.3799 ±0.0112	0.5306 ±0.0150	0.6360 ±0.0177	0.6798 ±0.0436	88.0 ±0.5

these three metrics through the proportion of generated graphs that are simultaneously valid, unique and novel (V.U.N.).

Constraining Criteria Various constraining criteria are chosen for ConStruct according to the structural properties of each dataset. For the planar dataset, we use planarity. For the tree dataset, we impose the absence of cycles. For the lobster dataset, we constrain the graph domain to those graphs whose connected components are lobsters. To check to what extent these criteria are verified by the compared methods, we compute the proportion of generated graphs that comply with the selected constraining criterion of the corresponding dataset (listed under the “Property” column in Table 1).

Graph Generation Performance We present the results in Table 1. For the planar dataset, ConStruct achieves nearly optimal performance, clearly outperforming all other methods. It is actually the first method to achieve 100% V.U.N., indicating state-of-the-art performance. Moreover, in terms of average ratio, it clearly outperforms all other methods, with the average ratio approaching 1, suggesting high sample quality. Regarding the lobster dataset, ConStruct exhibits a similar trend, demonstrating superior performance compared to DiGress+. It leads to state-of-the-art results in both average ratio and V.U.N. metrics. The lower novelty and uniqueness values ($<100\%$) are attributed to the dataset’s smaller size. In fact, we train both models on 64 examples (80% of the train set) while generating 100 graphs in each run. Conversely, for the tree dataset, ConStruct is outperformed by DiGress+ due to the marginally lower expressivity of the edge-absorbing noise model for this particular case (see Appendix H.1 for details). As a sanity check, we observe that for all three datasets, ConStruct ensures the constraining property for all generated graphs. However, the validity values are below 100% (except for planar) since connectedness of the graph is not guaranteed. In general, this property is not ensured by one-shot models and cannot be included as a constraining property since it is not edge-deletion invariant.

4.2 Digital Pathology Cell Graphs

Setup In the next set of experiments, we explore digital pathology data. Due to their natural representation of relational data, graphs are widely used to capture spatial biological dependencies from tissue images. We focus on cell graphs, whose nodes represent biological cells and edges serve as proxies for local cell-cell interactions. We build these structures from the genomic and clinical data available from the Molecular Taxonomy of Breast Cancer International Consortium (METABRIC) molecular dataset [12, 65, 14]. Each node is attributed with one of the nine possible phenotypes, which extensively characterizes a cell both anatomically and physiologically (more details in Appendix F.2). Regarding edges, we followed the typical procedure for cell graphs in digital pathology [34, 35, 2, 80]: first we employ Delaunay triangulation on the cell positions to construct the graphs, followed by edge thresholding to discard long edges. Our focus lies on generating biologically meaningful Tertiary Lymphoid Structures (TLSs), further described in Appendix F.3. Thus, we extract non-overlapping 4-hop subgraphs centered at nodes whose class is “B” from the whole-slide graphs. In terms of dimensionality, we obtain graphs with $b = 9$, corresponding to the 9 phenotypes detailed in Appendix F.2, and $c = 1$. We explore two datasets: one comprising graphs with high TLS content

and another consisting of graphs with low TLS content, based on domain-specific metrics (see below). We provide their statistic in Appendix F.4. We open-source both of them, representing to the best of our knowledge the first open-source digital pathology datasets specifically tailored for graph generation. For the sake of comparison, besides ConStruct and DiGress+, we implement a non deep learning baseline method proposed in [51] for this setting, which essentially captures 1-hop dependencies of cell graphs (see Appendix F.5). Additionally, we run BiGG [13], GraphGen [23], and SPECTRE [53]. These are the methods that, besides DiGress, attain non-zero V.U.N. for the planar dataset in Table 1, which we consider a proxy for performance in the digital pathology datasets due to the structural similarities between the datasets.

Metrics The *TLS embedding*, $\kappa = [\kappa_0, \dots, \kappa_5] \in \mathbb{R}^6$, has been proposed to quantify the TLS content in a cell graph [67, 51]. See Appendix F.3 for more details. Based on this metric, we define a graph G to contain low TLS content if $k_1(G) < 0.05$ and with high TLS content $k_2(G) > 0.05$ [51]. To evaluate the generative performance, we adopt the average ratio for structural graph statistics (Ratio) and V.U.N. metrics used in Section 4.1. Here we consider a planar and connected graph as a valid graph. Thus, we present explicitly the proportion of generated graphs that are connected (Conn.) and (Planar). Furthermore, for a biologically meaningful evaluation of the generated cell graphs, we use the domain metrics. We report the MMD between the distributions of the components of κ . We also consider the proportion of graphs that are planar, connected, and verify the low or high TLS content condition (TLS Valid), depending on the train set used.

Constraining criterion We use graph planarity as target structural property for ConStruct, as cell graphs are extracted from tissue slides using Delaunay triangulation, thus necessarily planar.

Results ConStruct outperforms all the baselines for all the summary evaluation metrics (in light gray in Table 2) for cell graph generation in both datasets. Unlike the synthetic datasets, here the structural distribution is conditioned on the node types, which is inherently a more complex task. This complexity contributes to the poor performance of the several unconstrained models. Constraining the edge generation process allows to significantly alleviate this modelling complexity, highlighting the benefits of ConStruct in such scenarios. We emphasize the substantial improvement in the V.U.N. of the generated graphs, with values approaching 100% using our framework, which aligns with the main motivation behind the proposed method. Interestingly, it also promotes the generation of more connected graphs. Finally, the 1-hop baseline model, while capturing the node type dependencies to some extent, as illustrated by the MMD on the components of κ , fails completely to capture structure based dependencies.

Additionally, we carry out some experiments for molecular datasets in Appendix G: we explore the utilization of planarity for constrained molecular generation and showcase how ConStruct can be used for controlled generation. Finally, we explore likelihood-based variants of ConStruct as well as some ablations to the projector in Appendix H.

5 Conclusion

In this paper, we introduced ConStruct, a framework that allows to integrate domain knowledge via structural constraints into graph diffusion models. By constraining the diffusion process based on a diverse set of geometric properties, we enable the generation of realistic graphs in scenarios with limited data. To accomplish that, we leverage on an edge-absorbing noise model and a projector operator to ensure that both the forward and reverse processes maintain the validity of sampled graphs within the constrained domain. Despite its algorithmic simplicity, our approach overcomes the arbitrarily hard problem of projecting a given graph into a combinatorial subspace in an efficient and theoretically grounded manner. Through several experiments on benchmark datasets, we showcase the versatility of ConStruct across various structural constraints. For example, in digital pathology datasets, our method outperforms existing approaches, bringing the validity of the generated graphs close to 100%. The incorporation of constraining properties jointly dependent on node and edges, as well as further exploitation of the induced sparsity by the edge-absorbing noise model may offer promising extensions to ConStruct.

References

- [1] Bijaya Adhikari, Bryan Lewis, Anil Vullikanti, José Mauricio Jiménez, and B Aditya Prakash. Fast and near-optimal monitoring for healthcare acquired infection outbreaks. *PLoS computational biology*, 15(9):e1007284, 2019. [1](#), [4](#)
- [2] David Ahmedt-Aristizabal, Mohammad Ali Armin, Simon Denman, Clinton Fookes, and Lars Petersson. A survey on graph-based deep learning for computational histopathology. *Computerized Medical Imaging and Graphics*, 95:102027, 2022. [8](#), [26](#)
- [3] Jacob Austin, Daniel D Johnson, Jonathan Ho, Daniel Tarlow, and Rianne Van Den Berg. Structured denoising diffusion models in discrete state-spaces. *Advances in Neural Information Processing Systems*, 34:17981–17993, 2021. [5](#), [32](#)
- [4] Davide Bacciu and Marco Podda. Graphgen-redux: A fast and lightweight recurrent model for labeled graph generation. In *2021 International Joint Conference on Neural Networks (IJCNN)*, pages 1–8. IEEE, 2021. [7](#), [25](#)
- [5] Kaustav Bera, Kurt A Schalper, David L Rimm, Vamsidhar Velcheti, and Anant Madabhushi. Artificial intelligence in digital pathology—new tools for diagnosis and precision oncology. *Nature reviews Clinical oncology*, 16(11):703–715, 2019. [26](#)
- [6] Andreas Bergmeister, Karolis Martinkus, Nathanaël Perraudin, and Roger Wattenhofer. Efficient and scalable graph generation through iterative local expansion. *The Twelfth International Conference on Learning Representations*, 2023. [2](#), [3](#), [7](#), [23](#), [25](#)
- [7] Sandeep N Bhatt and Frank Thomson Leighton. A framework for solving vlsi graph layout problems. *Journal of Computer and System Sciences*, 28(2):300–343, 1984. [4](#)
- [8] Nathan Brown, Marco Fiscato, Marwin HS Segler, and Alain C Vaucher. Guacamol: benchmarking models for de novo molecular design. *Journal of chemical information and modeling*, 59(3):1096–1108, 2019. [30](#)
- [9] Xiaohui Chen, Jiaying He, Xu Han, and Li-Ping Liu. Efficient and degree-guided graph generation via discrete diffusion modeling. *arXiv preprint arXiv:2305.04111*, 2023. [2](#), [3](#), [7](#), [25](#)
- [10] Markus Chimani, Ivo Hedtke, and Tilo Wiedera. Exact algorithms for the maximum planar subgraph problem: New models and experiments. *Journal of Experimental Algorithmics (JEA)*, 24:1–21, 2019. [6](#)
- [11] Jacob K Christopher, Stephen Baek, and Ferdinando Fioretto. Projected generative diffusion models for constraint satisfaction. *arXiv preprint arXiv:2402.03559*, 2024. [3](#)
- [12] Christina Curtis, Sohrab P Shah, Suet-Feung Chin, Gulisa Turashvili, Oscar M Rueda, Mark J Dunning, Doug Speed, Andy G Lynch, Shamith Samarajiwa, Yinyin Yuan, et al. The genomic and transcriptomic architecture of 2,000 breast tumours reveals novel subgroups. *Nature*, 486(7403):346–352, 2012. [8](#), [26](#)
- [13] Hanjun Dai, Azade Nazi, Yujia Li, Bo Dai, and Dale Schuurmans. Scalable deep generative modeling for sparse graphs. In *International conference on machine learning*, pages 2302–2312. PMLR, 2020. [3](#), [7](#), [8](#), [9](#), [25](#)
- [14] Esther Danenberg, Helen Bardwell, Vito RT Zanotelli, Elena Provenzano, Suet-Feung Chin, Oscar M Rueda, Andrew Green, Emad Rakha, Samuel Aparicio, Ian O Ellis, et al. Breast tumor microenvironment structures are associated with genomic features and clinical outcome. *Nature genetics*, 54(5):660–669, 2022. [8](#), [26](#)
- [15] Nicola De Cao and Thomas Kipf. Molgan: An implicit generative model for small molecular graphs. *arXiv preprint arXiv:1805.11973*, 2018. [3](#)
- [16] Nathaniel Lee Diamant, Alex M Tseng, Kangway V Chuang, Tommaso Biancalani, and Gabriele Scalia. Improving graph generation by restricting graph bandwidth. In *International Conference on Machine Learning*, pages 7939–7959. PMLR, 2023. [7](#), [25](#)

- [17] Marie-Caroline Dieu-Nosjean, Nicolas A Giraldo, Hélène Kaplon, Claire Germain, Wolf Herman Fridman, and Catherine Sautès-Fridman. Tertiary lymphoid structures, drivers of the anti-tumor responses in human cancers. *Immunological reviews*, 271(1):260–275, 2016. [2](#), [26](#)
- [18] Radoslav Dimitrov, Zeyang Zhao, Ralph Abboud, and Ismail Ceylan. Plane: Representation learning over planar graphs. *Advances in Neural Information Processing Systems*, 36, 2024. [30](#), [31](#)
- [19] Vijay Prakash Dwivedi and Xavier Bresson. A generalization of transformer networks to graphs. *arXiv preprint arXiv:2012.09699*, 2020. [16](#)
- [20] Kianoush Falahkheirkhah, Alex Lu, David Alvarez-Melis, and Grace Huynh. Domain adaptation using optimal transport for invariant learning using histopathology datasets. *arXiv preprint arXiv:2303.02241*, 2023. [26](#)
- [21] Nic Fishman, Leo Klarner, Valentin De Bortoli, Emile Mathieu, and Michael Hutchinson. Diffusion models for constrained domains. *arXiv preprint arXiv:2304.05364*, 2023. [4](#)
- [22] Nic Fishman, Leo Klarner, Emile Mathieu, Michael Hutchinson, and Valentin De Bortoli. Metropolis sampling for constrained diffusion models. *arXiv preprint arXiv:2307.05439*, 2023. [4](#)
- [23] Nikhil Goyal, Harsh Vardhan Jain, and Sayan Ranu. Graphgen: A scalable approach to domain-agnostic labeled graph generation. In *Proceedings of The Web Conference 2020*, pages 1253–1263, 2020. [7](#), [8](#), [9](#), [25](#)
- [24] T Ryan Gregory. Understanding evolutionary trees. *Evolution: Education and Outreach*, 1(2): 121–137, 2008. [4](#)
- [25] Cigdem Gunduz, Bülent Yener, and S Humayun Gultekin. The cell graphs of cancer. *Bioinformatics*, 20(suppl_1):i145–i151, 2004. [1](#), [26](#)
- [26] Kilian Konstantin Haefeli, Karolis Martinkus, Nathanaël Perraudin, and Roger Wattenhofer. Diffusion models for graphs benefit from discrete state spaces. *arXiv preprint arXiv:2210.01549*, 2022. [2](#), [3](#), [4](#)
- [27] Beth A Helmink, Sangeetha M Reddy, Jianjun Gao, Shaojun Zhang, Rafet Basar, Rohit Thakur, Keren Yizhak, Moshe Sade-Feldman, Jorge Blando, Guangchun Han, et al. B cells and tertiary lymphoid structures promote immunotherapy response. *Nature*, 577(7791):549–555, 2020. [2](#), [26](#)
- [28] Jonathan Ho, Ajay Jain, and Pieter Abbeel. Denoising diffusion probabilistic models. *Advances in neural information processing systems*, 33:6840–6851, 2020. [2](#)
- [29] John Hopcroft and Robert Tarjan. Efficient planarity testing. *Journal of the ACM (JACM)*, 21(4):549–568, 1974. [6](#), [22](#)
- [30] Han Huang, Leilei Sun, Bowen Du, and Weifeng Lv. Conditional diffusion based on discrete graph structures for molecular graph generation. In *Proceedings of the AAAI Conference on Artificial Intelligence*, volume 37, pages 4302–4311, 2023. [3](#)
- [31] Hankyu Jang, Samuel Justice, Philip M Polgreen, Alberto M Segre, Daniel K Sewell, and Sriram V Pemmaraju. Evaluating architectural changes to alter pathogen dynamics in a dialysis unit: for the cdc mind-healthcare group. In *Proceedings of the 2019 IEEE/ACM International Conference on Advances in Social Networks Analysis and Mining*, pages 961–968, 2019. [1](#), [4](#)
- [32] Yunhui Jang, Dongwoo Kim, and Sungsoo Ahn. Graph generation with K^2 -trees. In *The Twelfth International Conference on Learning Representations*, 2023. [7](#), [25](#)
- [33] Yunhui Jang, Seul Lee, and Sungsoo Ahn. A simple and scalable representation for graph generation. *arXiv preprint arXiv:2312.02230*, 2023. [7](#), [25](#)
- [34] Guillaume Jaume, Pushpak Pati, Valentin Anklin, Antonio Foncubierto, and Maria Gabrani. Histocartography: A toolkit for graph analytics in digital pathology. In *MICCAI Workshop on Computational Pathology*, pages 117–128. PMLR, 2021. [4](#), [8](#), [26](#)

- [35] Guillaume Jaume, Pushpak Pati, Behzad Bozorgtabar, Antonio Foncubierta, Anna Maria Anniciello, Florinda Feroce, Tilman Rau, Jean-Philippe Thiran, Maria Gabrani, and Orcun Goksel. Quantifying explainers of graph neural networks in computational pathology. In *Proceedings of the IEEE/CVF conference on computer vision and pattern recognition*, pages 8106–8116, 2021. [8](#), [26](#)
- [36] Wengong Jin, Regina Barzilay, and Tommi Jaakkola. Junction tree variational autoencoder for molecular graph generation. In *International conference on machine learning*, pages 2323–2332. PMLR, 2018. [3](#)
- [37] Jaehyeong Jo, Seul Lee, and Sung Ju Hwang. Score-based generative modeling of graphs via the system of stochastic differential equations. In *International Conference on Machine Learning*, pages 10362–10383. PMLR, 2022. [3](#), [4](#), [7](#), [25](#)
- [38] Laya Jose, Sidong Liu, Carlo Russo, Annemarie Nadort, and Antonio Di Ieva. Generative adversarial networks in digital pathology and histopathological image processing: A review. *Journal of Pathology Informatics*, 12(1):43, 2021. [26](#)
- [39] Thomas N Kipf and Max Welling. Variational graph auto-encoders. *arXiv preprint arXiv:1611.07308*, 2016. [3](#)
- [40] Lingkai Kong, Jiaming Cui, Haotian Sun, Yuchen Zhuang, B Aditya Prakash, and Chao Zhang. Autoregressive diffusion model for graph generation. In *International Conference on Machine Learning*, pages 17391–17408. PMLR, 2023. [2](#), [3](#)
- [41] Igor Krawczuk, Pedro Abranches, Andreas Loukas, and Volkan Cevher. Gg-gan: A geometric graph generative adversarial network. 2020. [3](#)
- [42] Johannes A La Poutr . Alpha-algorithms for incremental planarity testing (preliminary version). In *Proceedings of the twenty-sixth annual ACM symposium on Theory of Computing*, pages 706–715, 1994. [6](#), [22](#)
- [43] Hee Jin Lee, In Ah Park, In Hye Song, Su-Jin Shin, Joo Young Kim, Jong Han Yu, and Gyungyub Gong. Tertiary lymphoid structures: prognostic significance and relationship with tumour-infiltrating lymphocytes in triple-negative breast cancer. *Journal of clinical pathology*, 2015. [2](#), [26](#)
- [44] Xujia Li, Yuan Li, Xueying Mo, Hebing Xiao, Yanyan Shen, and Lei Chen. Diga: Guided diffusion model for graph recovery in anti-money laundering. In *Proceedings of the 29th ACM SIGKDD Conference on Knowledge Discovery and Data Mining*, pages 4404–4413, 2023. [1](#)
- [45] Renjie Liao, Yujia Li, Yang Song, Shenlong Wang, Will Hamilton, David K Duvenaud, Raquel Urtasun, and Richard Zemel. Efficient graph generation with graph recurrent attention networks. *Advances in neural information processing systems*, 32, 2019. [3](#), [7](#), [23](#), [25](#)
- [46] Phillip Lippe and Efstratios Gavves. Categorical normalizing flows via continuous transformations. *arXiv preprint arXiv:2006.09790*, 2020. [3](#)
- [47] Jenny Liu, Aviral Kumar, Jimmy Ba, Jamie Kiros, and Kevin Swersky. Graph normalizing flows. *Advances in Neural Information Processing Systems*, 32, 2019. [3](#)
- [48] Ilya Loshchilov and Frank Hutter. Decoupled weight decay regularization. In *International Conference on Learning Representations*, 2018. [23](#)
- [49] Aaron Lou and Stefano Ermon. Reflected diffusion models. *arXiv preprint arXiv:2304.04740*, 2023. [4](#)
- [50] Youzhi Luo, Keqiang Yan, and Shuiwang Ji. Graphdf: A discrete flow model for molecular graph generation. In *International Conference on Machine Learning*, pages 7192–7203. PMLR, 2021. [3](#)
- [51] Manuel Madeira, Dorina Thanou, and Pascal Frossard. Tertiary lymphoid structures generation through graph-based diffusion. In *International Conference on Medical Image Computing and Computer-Assisted Intervention*, pages 37–53. Springer, 2023. [2](#), [8](#), [9](#), [26](#), [27](#), [28](#)

- [52] Kaushalya Madhawa, Katushiko Ishiguro, Kosuke Nakago, and Motoki Abe. Graphnvp: An invertible flow model for generating molecular graphs. *arXiv preprint arXiv:1905.11600*, 2019. [3](#)
- [53] Karolis Martinkus, Andreas Loukas, Nathanaël Perraudin, and Roger Wattenhofer. Spectre: Spectral conditioning helps to overcome the expressivity limits of one-shot graph generators. In *International Conference on Machine Learning*, pages 15159–15179. PMLR, 2022. [3](#), [7](#), [8](#), [9](#), [23](#), [25](#)
- [54] Rocío Mercado, Tobias Rastemo, Edvard Lindelöf, Günter Klambauer, Ola Engkvist, Hongming Chen, and Esben Jannik Bjerrum. Graph networks for molecular design. *Machine Learning: Science and Technology*, 2(2):025023, 2021. [1](#)
- [55] Puria Azadi Moghadam, Sanne Van Dalen, Karina C Martin, Jochen Lennerz, Stephen Yip, Hossein Farahani, and Ali Bashashati. A morphology focused diffusion probabilistic model for synthesis of histopathology images. In *Proceedings of the IEEE/CVF Winter Conference on Applications of Computer Vision*, pages 2000–2009, 2023. [26](#)
- [56] Christopher Morris, Martin Ritzert, Matthias Fey, William L Hamilton, Jan Eric Lenssen, Gaurav Rattan, and Martin Grohe. Weisfeiler and leman go neural: Higher-order graph neural networks. In *Proceedings of the AAAI conference on artificial intelligence*, volume 33, pages 4602–4609, 2019. [16](#)
- [57] Luis Munoz-Erazo, Janet L Rhodes, Valentine C Marion, and Roslyn A Kemp. Tertiary lymphoid structures in cancer—considerations for patient prognosis. *Cellular & molecular immunology*, 17(6):570–575, 2020. [2](#), [26](#)
- [58] Alexander Quinn Nichol and Prafulla Dhariwal. Improved denoising diffusion probabilistic models. In *International Conference on Machine Learning*, pages 8162–8171. PMLR, 2021. [5](#)
- [59] Chenhao Niu, Yang Song, Jiaming Song, Shengjia Zhao, Aditya Grover, and Stefano Ermon. Permutation invariant graph generation via score-based generative modeling. In *International Conference on Artificial Intelligence and Statistics*, pages 4474–4484. PMLR, 2020. [3](#)
- [60] Costantino Pitzalis, Gareth W Jones, Michele Bombardieri, and Simon A Jones. Ectopic lymphoid-like structures in infection, cancer and autoimmunity. *Nature Reviews Immunology*, 14(7):447–462, 2014. [26](#)
- [61] Daniil Polykovskiy, Alexander Zhebrak, Benjamin Sanchez-Lengeling, Sergey Golovanov, Oktai Tatanov, Stanislav Belyaev, Rauf Kurbanov, Aleksey Artamonov, Vladimir Aladinskiy, Mark Veselov, et al. Molecular sets (moses): a benchmarking platform for molecular generation models. *Frontiers in pharmacology*, 11:565644, 2020. [30](#)
- [62] Kristina Preuer, Philipp Renz, Thomas Unterthiner, Sepp Hochreiter, and Gunter Klambauer. Fréchet chemnet distance: a metric for generative models for molecules in drug discovery. *Journal of chemical information and modeling*, 58(9):1736–1741, 2018. [30](#)
- [63] Yiming Qin, Clement Vignac, and Pascal Frossard. Sparse training of discrete diffusion models for graph generation. *arXiv preprint arXiv:2311.02142*, 2023. [2](#), [3](#), [16](#)
- [64] Sashank J Reddi, Satyen Kale, and Sanjiv Kumar. On the convergence of adam and beyond. In *International Conference on Learning Representations*, 2018. [23](#)
- [65] Oscar M Rueda, Stephen-John Sammut, Jose A Seoane, Suet-Feung Chin, Jennifer L Caswell-Jin, Maurizio Callari, Rajbir Batra, Bernard Pereira, Alejandra Bruna, H Raza Ali, et al. Dynamics of breast-cancer relapse reveal late-recurring er-positive genomic subgroups. *Nature*, 567(7748):399–404, 2019. [8](#), [26](#)
- [66] Alberto Sanfeliu and King-Sun Fu. A distance measure between attributed relational graphs for pattern recognition. *IEEE transactions on systems, man, and cybernetics*, (3):353–362, 1983. [5](#), [18](#)

- [67] Nadine S Schaadt, Ralf Schönmeyer, Germain Forestier, Nicolas Brieu, Peter Braubach, Katharina Nekolla, Michael Meyer-Hermann, and Friedrich Feuerhake. Graph-based description of tertiary lymphoid organs at single-cell level. *PLoS computational biology*, 16(2):e1007385, 2020. [1](#), [2](#), [9](#), [26](#), [27](#)
- [68] Claire Seibold and Hannah L Callender. Modeling epidemics on a regular tree graph. *Letters in Biomathematics*, 3(1):59–74, 2016. [4](#)
- [69] Ahmed Serag, Adrian Ion-Margineanu, Hammad Qureshi, Ryan McMillan, Marie-Judith Saint Martin, Jim Diamond, Paul O’Reilly, and Peter Hamilton. Translational ai and deep learning in diagnostic pathology. *Frontiers in medicine*, 6:185, 2019. [26](#)
- [70] Kartik Sharma, Srijan Kumar, and Rakshit Trivedi. Plug-and-play controllable graph generation with diffusion models. In *ICML 2023 Workshop on Structured Probabilistic Inference \& Generative Modeling*, 2023. [3](#)
- [71] Howard E Simmons III and John E Maggio. Synthesis of the first topologically non-planar molecule. *Tetrahedron Letters*, 22(4):287–290, 1981. [4](#)
- [72] Martin Simonovsky and Nikos Komodakis. Graphvae: Towards generation of small graphs using variational autoencoders. In *Artificial Neural Networks and Machine Learning–ICANN 2018: 27th International Conference on Artificial Neural Networks, Rhodes, Greece, October 4-7, 2018, Proceedings, Part I* 27, pages 412–422. Springer, 2018. [3](#)
- [73] Jascha Sohl-Dickstein, Eric Weiss, Niru Maheswaranathan, and Surya Ganguli. Deep unsupervised learning using nonequilibrium thermodynamics. In *International conference on machine learning*, pages 2256–2265. PMLR, 2015. [2](#)
- [74] Zhiqing Sun and Yiming Yang. Difusco: Graph-based diffusion solvers for combinatorial optimization. *Advances in Neural Information Processing Systems*, 36, 2024. [1](#)
- [75] Alex M Tseng, Nathaniel Diamant, Tommaso Biancalani, and Gabriele Scalia. Complex preferences for different convergent priors in discrete graph diffusion. *arXiv preprint arXiv:2306.02957*, 2023. [32](#)
- [76] Clement Vignac and Pascal Frossard. Top-n: Equivariant set and graph generation without exchangeability. *arXiv preprint arXiv:2110.02096*, 2021. [3](#), [31](#)
- [77] Clement Vignac, Igor Krawczuk, Antoine Siraudin, Bohan Wang, Volkan Cevher, and Pascal Frossard. Digress: Discrete denoising diffusion for graph generation. *arXiv preprint arXiv:2209.14734*, 2022. [2](#), [3](#), [4](#), [5](#), [7](#), [16](#), [25](#), [30](#), [31](#)
- [78] Clement Vignac, Nagham Osman, Laura Toni, and Pascal Frossard. Midi: Mixed graph and 3d denoising diffusion for molecule generation. In *Joint European Conference on Machine Learning and Knowledge Discovery in Databases*, pages 560–576. Springer, 2023. [30](#)
- [79] Zhenqin Wu, Bharath Ramsundar, Evan N Feinberg, Joseph Gomes, Caleb Geniesse, Aneesh S Pappu, Karl Leswing, and Vijay Pande. Moleculenet: a benchmark for molecular machine learning. *Chemical science*, 9(2):513–530, 2018. [30](#)
- [80] Zhenqin Wu, Alexandro E Trevino, Eric Wu, Kyle Swanson, Honesty J Kim, H Blaize D’Angio, Ryan Preska, Gregory W Charville, Piero D Dalerba, Ann Marie Egloff, et al. Graph deep learning for the characterization of tumour microenvironments from spatial protein profiles in tissue specimens. *Nature Biomedical Engineering*, 6(12):1435–1448, 2022. [8](#), [26](#)
- [81] Feng Xie and David Levinson. Topological evolution of surface transportation networks. *Computers, Environment and Urban Systems*, 33(3):211–223, 2009. [4](#)
- [82] Keyulu Xu, Weihua Hu, Jure Leskovec, and Stefanie Jegelka. How powerful are graph neural networks? *arXiv preprint arXiv:1810.00826*, 2018. [16](#)
- [83] Qi Yan, Zhengyang Liang, Yang Song, Renjie Liao, and Lele Wang. Swingnn: Rethinking permutation invariance in diffusion models for graph generation. *arXiv preprint arXiv:2307.01646*, 2023. [3](#)

- [84] Kai Yi, Bingxin Zhou, Yiqing Shen, Pietro Liò, and Yuguang Wang. Graph denoising diffusion for inverse protein folding. *Advances in Neural Information Processing Systems*, 36, 2024. [1](#)
- [85] Jiaxuan You, Rex Ying, Xiang Ren, William Hamilton, and Jure Leskovec. Graphrnn: Generating realistic graphs with deep auto-regressive models. In *International conference on machine learning*, pages 5708–5717. PMLR, 2018. [3](#), [7](#), [25](#)

A Graph Discrete Diffusion Model

In this section, we further detail the design of the graph discrete diffusion model used to illustrate the constraining framework of ConStruct.

A.1 Parameterization of the Reverse Process

The distribution $p_\theta(G^{t-1}|G^t)$ fully defines the reverse process. Under an independence assumption between nodes and edges, this distribution can be modelled as:

$$p_\theta(G^{t-1}|G^t) = \prod_{1 \leq i \leq n} p_\theta(x_i^{t-1}|G^t) \prod_{1 \leq i, j \leq n} p_\theta(e_{ij}^{t-1}|G^t). \quad (4)$$

To compute each of these terms, we use the GNN_θ predictions through the following marginalization:

$$p_\theta(x_i^{t-1}|G^t) = \sum_{x \in \mathcal{X}} p_\theta(x_i^{t-1}|x_i = x, G^t) \hat{p}_i^X(x), \quad (5)$$

where $\hat{p}_i^X(x)$ denotes the GNN_θ predicted probability of node i being of type x . Similarly, for the edges we have $p_\theta(e_{ij}^{t-1}|G^t) = \sum_{e \in \mathcal{E}} p_\theta(e_{ij}^{t-1}|e_{ij} = e, G^t) \hat{p}_{ij}^E(e)$. To compute the missing term in Equation (5), we equate it to the posterior term of the forward process:

$$\begin{aligned} p_\theta(x_i^{t-1}|x_i = x, G^t) &= \\ &= \begin{cases} \frac{\mathbf{x}_i^t(\mathbf{Q}_X^t)' \odot \mathbf{x}_i \mathbf{Q}_X^{t-1}}{\mathbf{x}_i^t \mathbf{Q}_X^t \mathbf{x}_i} & \text{if } q(x_i^t|x_i = x) > 0, \\ 0 & \text{otherwise,} \end{cases} \end{aligned} \quad (6)$$

where $'$ denotes transposition.

To endow the graph diffusion model of the desired equivariance properties, a Graph Neural Network, GNN_θ , is used as the denoising neural network, along with a permutation invariant loss (see Appendix A.2). In terms of architecture, we adopt the exact same denoising network architecture of DiGress [77], a Graph Transformer [19].

Importantly, the edge-absorbing noise model used in ConStruct increases graph sparsity throughout the forward trajectory. Consequently, beyond the distribution preserving guarantees, it also allows for the efficient computation of extra features on the noisy graphs that otherwise the GNN_θ would not be able to capture. Following Vignac et al. [77], these are fed as an additional input to the denoising network (see Algorithm 1 and Algorithm 2), further enhancing its expressivity beyond the well-known limited representational power of GNN architectures [82, 56]. More concretely, besides the spectral (eigenvalues and eigenvectors of the Laplacian) and structural (number of cycles) features from DiGress, we also consider some additional features. We add as graph features the degree distribution and the node and edge type distributions. While the former enhances the positional information within the graph, the latter helps in making more explicit to the model the prevalence of each class in the dataset. Additionally, we add auxiliary structural encodings to edges to boost edge label prediction. We compute the Adamic-Adar index to aggregate local neighborhood information and the shortest distance between nodes to encode node interactions. For computational limitations, we only consider information within a 10-hop radius for these computations. These additional features were previously proposed by Qin et al. [63].

A.2 Training Algorithm

The chosen denoising graph neural network GNN_θ is trained using the cross-entropy loss between its predicted probabilities for each node and edge types, $\hat{p}^G = (\hat{p}^X, \hat{p}^E)$ and the actual node and edge types of a clean graph, $\mathbf{G} = (\mathbf{X}, \mathbf{E})$:

$$L(\hat{p}^G, G) = \text{CE}(\hat{p}^X, \mathbf{X}) + \lambda \text{CE}(\hat{p}^E, \mathbf{E}), \quad (7)$$

where λ is an hyperparameter that is tuned to balance both loss terms.

This loss is permutation invariant. Thus, if we also consider an equivariant architecture (e.g. the one described in Appendix A.1), the diffusion model is endowed of the desired equivariance properties.

This allows the model to dodge the node ordering sensitivity from which, for example, autoregressive models suffer.

Given these two components, all the necessary elements are in place for the training of the diffusion model, which is defined in Algorithm 1.

Algorithm 1: Training Algorithm for Graph Discrete Diffusion Model

Input: Graph dataset \mathcal{D}

```

1 repeat
2   Sample  $G = (\mathbf{X}, \mathbf{E}) \sim \mathcal{D}$ ;
3   Sample  $t \sim \mathcal{U}(1, \dots, T)$ ;
4   Sample  $G^t \sim \mathbf{X} \mathbf{Q}_X^t \times \mathbf{E} \mathbf{Q}_E^t$ ;
5    $h \leftarrow f(G^t, t)$ ; // Compute extra features
6    $\hat{p}^X, \hat{p}^E \leftarrow \text{GNN}_\theta(G^t, h)$ ;
7    $\text{loss} \leftarrow \text{CE}(\hat{p}^X, \mathbf{X}) + \lambda \text{CE}(\hat{p}^E, \mathbf{E})$ ;
8    $\text{optimizer.step}(\text{loss})$ ;
9 until convergence of  $\text{GNN}_\theta$ ;
```

A.3 Sampling Algorithm

In this section, we present Construct’s proposed sampling algorithm, shown in Algorithm 2. At each timestep, we use the projector operator, described in Algorithm 3, to keep the sampled graphs throughout the reverse process within the constrained domain.

Algorithm 2: Sampling Algorithm for Constrained Graph Discrete Diffusion Model

Input: Number of graphs to sample N and constraining property P

```

1 for  $i = 1$  to  $N$  do
2   Sample  $n$  from the training set distribution;
3   Sample  $G^T \sim q_X(n) \times q_E(n)$ ; // Sample from limit distribution
4   for  $t = T$  to 1 do
5      $h \leftarrow f(G^t, t)$ ; // Compute extra features
6      $\hat{p}^X, \hat{p}^E \leftarrow \text{GNN}_\theta(G^t, h)$ ;
7      $\hat{G}^{t-1} \sim p_\theta(G^{t-1} | G^t)$ ; // Sample from distribution in Equation (4)
8      $G^{t-1} \leftarrow \text{Projector}(P, \hat{G}^{t-1}, G^t)$ ;
9   end
10  Store  $G^0$ ;
11 end
```

Algorithm 3: Projector

Input: Constraining property P , noisy graph $G^t = (X^t, E^t)$ and candidate graph

$$\hat{G}^{t-1} = (\hat{X}^{t-1}, \hat{E}^{t-1})$$

```

1  $G^{t-1} \leftarrow (\hat{X}^{t-1}, E^t)$ ;
2  $E' \leftarrow \hat{E}^{t-1} \setminus E^t$ ; // Get candidate edges
3 repeat
4   Sample  $e' \sim E'$ ;
5   if  $P(G^{t-1}.insert(e'))$  then
6      $G^{t-1} \leftarrow G^{t-1}.insert(e')$ ; // Insert only valid edges
7   end
8    $E' \leftarrow E' \setminus \{e'\}$ ;
9 until  $E' = \emptyset$ ;
10 return  $G^{t-1}$ ;
```

B Theoretical Analysis

In this section, we theoretically analyse the projector. We start by defining a notion of distance between graphs [66].

Definition B.1. Let G_1 and G_2 be two unattributed graphs. The graph edit distance with uniform cost, denoted by $\text{GED}(G_1, G_2)$, is defined as:

$$\text{GED}(G_1, G_2) = \min_{(e_1, \dots, e_k) \in \mathcal{E}(G_1, G_2)} \sum_{i=1}^k c(e_i) = \min_{(e_1, \dots, e_k) \in \mathcal{E}(G_1, G_2)} \alpha |(e_1, \dots, e_k)| \quad (8)$$

where $\mathcal{E}(g_1, g_2)$ denotes the set of edit paths that convert G_1 into G_2 (up to an isomorphism), $c(e) = \alpha > 0$ is the uniform cost of each usual set of elementary graph edit operators and $|(e_1, \dots, e_k)|$ refers to the cardinality of the edit path.

Importantly, in this analysis we choose GED due to its permutation invariance properties. We only define it over unattributed graphs for an objective evaluation as ConStruct only operates at the graph structural level. Moreover, as our generative process imposes a fixed number of nodes throughout the whole reverse process, the relevant elementary edits for GED are edge insertion and deletion.

Additionally, we use the notation $G \supset G'$ to denote that $G' = (X', E')$ is a subgraph of $G = (X, E)$, i.e., that up to an isomorphism, we have $E \supset E'$ and $X = X'$. For brevity, we slightly abuse notation and also define the union between a graph, $G = (X, E)$, and a set of edges, E' , to be the graph whose edges result from the union of its edges with those of the set, i.e., $G \cup E' = G' = (X, E \cup E')$. Similarly, we have $G \setminus E' = G' = (X, E \setminus E')$.

The next results are organized in the following way: the first theorem proves that for any edge-deletion invariant constraining property (Definition 3.1), our projector can retrieve a graph that results from a projection onto the constrained set under the GED sense. Then, we prove that when considering acyclicity as target structural property, the projector is guaranteed to output the optimal (projected) samples. We finally show that this second property does not hold for all edge-deletion invariant properties, giving counter-examples for the cases of planarity, maximum degree and lobster components.

Theorem 1. Let:

- P be the edge-deletion invariant Definition 3.1 constraining property of the projector;
- G^t be a noisy graph obtained at timestep t ;
- \hat{G}^{t-1} be a sampled graph from $p_\theta(G^{t-1}|G^t)$, i.e., the one-step denoised candidate graph directly proposed by the diffusion model when taking G^t as input;
- $\mathcal{G}^{t-1} = \text{Projector}(P, \hat{G}^{t-1}, G^t)$ be the set of all possible final one-step denoised graph outputted by ConStruct.

We define (G^*, e^*) any optimal solutions of the following optimization problem:

$$\min_{G \in \mathcal{C}} \text{GED}(\hat{G}^{t-1}, G) = \min_{G \in \mathcal{C}} \min_{(e_1, \dots, e_k) \in \mathcal{E}(\hat{G}^{t-1}, G)} \alpha |(e_1, \dots, e_k)|, \quad (9)$$

where $\mathcal{C} = \{G \in \mathcal{G} | P(G) = \text{True}, G \supset G^t\}$, with \mathcal{G} the set of all unattributed graphs. Then, (G^*, e^*) can be recovered by our projector, i.e. $G^* \in \mathcal{G}^{t-1}$.

Proof. If $\hat{G}^{t-1} \in \mathcal{C}$, the theorem is trivially verified since the output of the projector is directly \hat{G}^{t-1} , as well as the solution of the minimization problem. Therefore, for the rest of the proof, we only consider the case $\hat{G}^{t-1} \notin \mathcal{C}$.

Now, since the reverse process of the diffusion model is an edge insertion process, we have $\hat{G}^{t-1} = G^t \cup E_{\text{candidate}} \supset G^t$. Also, we notice that the projector amounts to randomly remove edges from \hat{G}^{t-1} until we find a graph within the constraint set (equivalently, it entails adding as many edges as possible to G^t while ensuring that the graph remains within the constraint set). Thus, it suffices to prove that for (G^*, e^*) we necessarily have an optimal edit path $e^* = (e_1^*, \dots, e_k^*)$ from \hat{G}^{t-1} to G^* exclusively composed of edge deletions. In this case, our projector can necessarily produce G^* .

Let (G^*, e^*) be such a solution, and define $G_{:,i}^*$ the graph resulting from the i^{th} first edits $e_{:,i}^* = (e_1^*, \dots, e_i^*)$ with $i \leq k$. We will prove by induction that, for all $1 \leq i \leq k$, $e_{:,i}^*$ is only composed of edge deletions such that $G^t \subset G_{:,i}^*$.

i = 1: Since $\hat{G}^{t-1} \notin \mathcal{C}$ and $\hat{G}^{t-1} \supset G^t$, we have that $P(\hat{G}^{t-1}) = \text{False}$. As P is edge-deletion invariant, inserting any set of edges E to \hat{G}^{t-1} implies that

$$P(\hat{G}^{t-1}) = \text{False} \implies P(\hat{G}^{t-1} \cup E) = \text{False}. \quad (10)$$

Therefore, we have:

$$\min_{G \in \mathcal{C}} \text{GED}(\hat{G}^{t-1}, G) = \min_{(G^t \cup E_G) \in \mathcal{C}} \text{GED}(G^t \cup E_{\text{candidate}}, G^t \cup E_G) \quad (11)$$

$$= \min_{(G^t \cup E_G) \in \mathcal{C}} \alpha |E_{\text{candidate}} \setminus E_G| \quad (12)$$

$$\leq \min_{(G^t \cup E_G) \in \mathcal{C}} \alpha |E_{\text{candidate}} \cup E \setminus E_G| \quad (13)$$

$$= \min_{(G^t \cup E_G) \in \mathcal{C}} \text{GED}(\hat{G}^{t-1} \cup E, G^t \cup E_G) \quad (14)$$

$$= \min_{G \in \mathcal{C}} \text{GED}(\hat{G}^{t-1} \cup E, G). \quad (15)$$

Thus, we conclude that any edge insertions would take us further away from the constraint set. Therefore, e_1^* cannot represent an edge insertion. However, it could still be an edge deletion such that $G^t \not\subset G_{:1}^*$. In this case, an extra edge insertion would be necessary to recover G^t in $G_{:1}^*$, which is required since $G^* \supset G^t$, i.e.,

$$\min_{G \in \mathcal{C}} \text{GED}(\hat{G}^{t-1}, G) \leq \min_{G \in \mathcal{C}} \text{GED}(G_{:1}^*, G). \quad (16)$$

Contrarily, if e_1^* is an edge deletion such that $G^t \subset G_{:1}^*$, we have:

$$\min_{G \in \mathcal{C}} \text{GED}(\hat{G}^{t-1}, G) > \min_{G \in \mathcal{C}} \text{GED}(G_{:1}^*, G), \quad (17)$$

since $G^t \subset G_{:1}^* \subset \hat{G}^{t-1}$. Therefore, we verify the intended property for $i = 1$.

1 < i ≤ k: We have $G_{:i-1}^* \notin \mathcal{C}$ because $P(G_{:i-1}^*) = \text{False}$. Otherwise $G_{:i-1}^*$ would be the solution since $G^t \subset G_{:i-1}^*$. Hence for any set of inserted edges E ,

$$\min_{G \in \mathcal{C}} \text{GED}(G_{:i-1}^*, G) \leq \min_{G \in \mathcal{C}} \text{GED}(G_{:i}^* \cup E, G), \quad (18)$$

implying that e_i^* is an edge deletion. By the same token, if $G^t \not\subset G_{:i}^*$, then necessarily an extra insertion edit would be necessary to recover G^t further in G^* , so we have again:

$$\min_{G \in \mathcal{C}} \text{GED}(G_{:i-1}^*, G) \leq \min_{G \in \mathcal{C}} \text{GED}(G_{:i}^*, G), \quad (19)$$

which, as seen before, is suboptimal. Thus, e_i^* is an edge deletion such that $G^t \subset G_{:i}^*$. By noticing that $G_{:k}^* = G^*$, we conclude our proof. This induction shows that only an edit path e^* composed of edge deletions such that all intermediate graphs contain G^t leads to an optimal projection w.r.t GED. \square

Critical analysis of the result in Theorem 1: See Section 3.4 for a critical analysis of this result.

In the following theorem we prove that the projector always picks the solution of the optimization problem, i.e., that any element of \mathcal{G}^{t-1} is actually a solution of the optimization problem in Theorem 1. In this proof, we use the concept of connected component of a graph, i.e., a subgraph of the given graph in which there is a path between any of its two vertices, but no path exists between any vertex in the subgraph and any vertex outside of it. Therefore, any edge inserted between two nodes in the same connected component leads to a cycle. Importantly, we trivially consider an isolated node as a connected component.

Theorem 2. *Under the same conditions of Theorem 1, if P returns true for graphs with no cycles, we have:*

$$\mathcal{G}^{t-1} = \operatorname{argmin}_{G \in \mathcal{C}} \text{GED}(\hat{G}^{t-1}, G).$$

Proof. Following the proof of Theorem 1, if we define again $\hat{G}^{t-1} = G^t \cup E_{\text{candidate}}$, we have:

$$\begin{aligned} \min_{G \in \mathcal{C}} \text{GED}(\hat{G}^{t-1}, G) &= \min_{(G^t \cup E_G) \in \mathcal{C}} \text{GED}(G^t \cup E_{\text{candidate}}, G^t \cup E_G) \\ &= \min_{\{E_G \mid P(G^t \cup E_G) = \text{True}, E_G \subset E_{\text{candidate}}\}} |E_{\text{candidate}} \setminus E_G| \\ &= \max_{\{E_G \mid P(G^t \cup E_G) = \text{True}, E_G \subset E_{\text{candidate}}\}} |E_G|, \end{aligned}$$

where the first equality is just a change of variables and the second comes from $E_{\text{candidate}} \supset E_G$, as shown in Theorem 1. This shows that a solution to $\text{argmin}_{G \in \mathcal{C}} \text{GED}(\hat{G}^{t-1}, G)$ maximizes the number of edges added to G^t . This is a general result under the conditions of Theorem 1 and not specific for graphs with no cycles. We now want to show that any element of \mathcal{G}^{t-1} is a solution to this optimization problem.

We define $|\text{CC}_{\text{candidate}}|$ as the number of distinct connected components of G^t reached by $E_{\text{candidate}}$. We remark that the considered graphs all have the same fixed number of nodes. A well-known result for graphs without cycles is that, under the provided setting, the maximum number of edges from $E_{\text{candidate}}$ that we can insert is $|\text{CC}_{\text{candidate}}| - 1$, i.e., we sequentially insert an edge per pair of separate connected components. Thus, we have:

$$\max_{\{E_G \mid P(G^t \cup E_G) = \text{True}, E_G \subset E_{\text{candidate}}\}} |E_G| \leq |\text{CC}_{\text{candidate}}| - 1.$$

On the other hand, the only edges from $E_{\text{candidate}}$ that the projector rejects are the ones creating cycles. This means that the refused edges would not reduce the number of separate connected components, since they would connect vertices already in the same connected component. Thus, for a graph $G_{\text{projector}} = G^t \cup E_{\text{projector}} \in \mathcal{G}^{t-1}$, we necessarily have:

$$|E_{\text{projector}}| = |\text{CC}_{\text{candidate}}| - 1,$$

which tightly matches the upper bound for the optimization problem seen above. Consequently, any $G_{\text{projector}} \in \mathcal{G}^{t-1}$ is necessarily solution of the optimization problem, i.e.:

$$\mathcal{G}^{t-1} \subset \text{argmin}_{G \in \mathcal{C}} \text{GED}(\hat{G}^{t-1}, G)$$

□

For other edge-deletion invariant properties, we provide examples of $G_{\text{projector}}$ with a different number of edges inserted by the projector, $|E_{\text{projector}}|$, in Figure 3. These are necessarily counter-examples to what was proved in Theorem 2 for acyclic graphs ($\mathcal{G}^{t-1} \subset \text{argmin}_{G \in \mathcal{C}} \text{GED}(\hat{G}^{t-1}, G)$). Nevertheless, the opposite relation still holds from Theorem 1.

Constraint	G^t	\hat{G}^{t-1}	G^{t-1}	$ E_{\text{Projector}} $
Planar				2
				1
Maximum Degree				2
				1
Lobster Components				6
				5

Figure 3: Examples of different G^{t-1} that can be yielded by $\text{Projector}(P, \hat{G}^{t-1}, G^t)$ for given P (column “Constraint”), G^t , and \hat{G}^{t-1} (columns with the respective name) that lead to the insertion of a different number of edges. For the maximum degree row, the example given considers that the maximum allowed degree is 2. For the column \hat{G}^{t-1} , the dashed lines represent the candidate edges. For the column G^{t-1} , the green lines denote the actually inserted edges by the projector.

C Incremental Algorithms

As discussed in Section 3.5, utilizing the projector in the edge insertion reverse process (i.e., $G^t \subset G^{t-1}$) allows us to further enhance efficiency by leveraging incremental algorithms for graph property satisfaction checking. These algorithms avoid performing a full property satisfaction check on the new graph at each timestep. Instead, they assume that the previous graph (i.e., before the new edge was added) already satisfies the target structural property. Incremental algorithms focus on verifying the impact of the newly added edge by updating and checking only the affected parts of smartly designed data structures. In other words, contrary to their full graph counterparts, incremental algorithms allow for property satisfaction checks at a local level. This approach accelerates the property satisfaction checking process by reducing redundant computation.

In this section, we discuss the incremental property satisfaction algorithms for the edge-deletion invariant properties analysed throughout the paper. We also note that due to the combinatorial nature of edge-deletion invariant properties, each property satisfaction algorithm is specific to the property in question. There is no general efficient property satisfaction checker for all edge-deletion invariant properties. Consequently, we address each property on a case-by-case basis.

Planar The best performing full property satisfaction algorithm known for planarity is $O(n)$ [29], while its fastest known incremental test has amortized running time of $O(\alpha(q, n))$ [42] (“almost constant” complexity), where q is the total number of operations (edge queries and insertions), and α denotes the inverse-Ackermann function.

Acyclicity In generic undirected graphs (our case), the usual full tests via DFS/BFS have a complexity of $O(|X| + |E|)$, i.e., the algorithms have to traverse the full graph to reject the existence of any cycle. However, for the dynamic case, given that G^t has no cycles, we can only check if the added edges, E_{added} , connect nodes already in the same connected component. This check can be efficiently performed if we keep an updated hashtable that maps each node to the index of the connected component it belongs at that iteration (an isolated node is a connected component) and another one with all the nodes belonging to each connected component. Whenever there is a new edge proposed, we check if the nodes are already in the same connected component. If not, we insert the edge and update the two hashtables accordingly; otherwise, we reject the edge since it would create a cycle. Therefore, the cycle check can be done in $O(|E_{\text{added}}|)$.

Lobster Components Its global test involves removing twice the leaves of the graph and checking if the remaining connected components are paths. This algorithm has a complexity of $O(|E|)$. For the incremental version, we can use a similar approach to that of the absence of cycles but additionally check if the newly connected node is not more than two hops away from the path in its connected component, as lobster graphs are specific instances of forest graphs. If, again, we keep track of the paths of each connected component in a hashtable, we still get an incremental algorithm of complexity $O(|E_{\text{added}}|)$ for this property.

Maximum Degree The optimal full property satisfaction algorithm has a complexity of $O(|X|)$ since it has to perform a degree check across all nodes. The incremental version is naturally just a quick check for nodes that are vertices of E_{added} . Again, if we keep an updated hashtable with the degree of each node, this can be quickly performed in $O(E_{\text{added}})$.

D Experimental Details

D.1 Training Details

As mentioned in Section 4, we follow the splits originally proposed for each of the unattributed datasets (lobster [45], planar [53], and tree [6]): 80% of the graphs are used in the training set and the remaining 20% are allocated to the test set. We use 20% of the train set as validation set. We note that for the lobster dataset, the original splits provided in the open-source code from Liao et al. [45] use the validation set as a subset of the train set, i.e., all the samples in the validation set are used to train. In contrast, we follow Martinkus et al. [53]’s protocol, isolating completely the validation samples from the train (again, 20% of the train split). In any case, the test splits are coincident between our approach and the one from Liao et al. [45]. For the digital pathology datasets, we follow the same protocol.

These splits and the hyperparameters used for each model are provided in the computational implementation of the paper as the default values for each of the experiments. For each configuration, we save the five best models in terms of negative log likelihood and the last one (for ConStruct, we compute the likelihood of the corresponding unconstrained model) and pick the best performing model across those six checkpoints. Regarding the optimizer, we used the AMSGrad [64] version of AdamW [48] with a learning rate of 0.0002 and weight decay of 1e-12 for all the experiments.

D.2 Resources

All our experiments were run in individual Nvidia V100 32Gb GPUs. We present the training and sampling times (total of 5 runs, 100 generated graphs each) for each dataset for the diffusion models in Table 3.

Table 3: Training times for the diffusion model in different datasets.

Dataset	Training Time (h)
Planar	48
Tree	44
Lobster	50
High TLS	61
Low TLS	61
QM9	9.5
MOSES	335.5
GuacaMol	502

The baseline model for the digital pathology dataset does not use any GPU. It takes 0.6s to train and 2 minutes to sample from. The sampling times for ConStruct can be found in Appendix D.3. As the order of magnitude of training times is significantly larger than the one of sampling times, Table 3 provides a good estimate of the total computational resources required for this paper.

D.3 Runtimes

A major advantage of our framework is that it does not interfere with the training of the diffusion model, preserving its efficiency, as discussed in the first paragraph of Section 3.5. Therefore, there is no overburden in the training time caused by ConStruct. For this reason, in this section we only analyse the different sampling runtimes. In particular, we track the sampling times of DiGress+ and the ones of ConStruct with and without the efficiency boosting components described in Section 3.5 (edge blocking hashtable and incremental property satisfaction algorithm).

Additionally, a natural procedure to ensure 100% constraint verification solely using DiGress+ is to first directly perform unconstrained generation and then applying a validation process to filter out the ones that do not verify the constraint. This *a posteriori* filtering requires a full graph property check, run only once after the graph has been generated but that is thus more computationally expensive when compared to their incremental versions employed by ConStruct. The complexity comparison between a full graph property check ran only once *vs* an incremental check for each

added edge is property specific. However, the main bottleneck of the *a posteriori* filtering is that it wastes computational resources in case of graph rejection (i.e., in the case of a graph not verifying the property, all the resources used in its generation and full graph property checking are wasted) and requires restarting the sampling from zero again with an additional property check at the end. Furthermore, this procedure has to be performed sequentially, since we can only check the graphs constraint satisfaction after their generation. ConStruct avoids such redundancy and, thus, waste of computation by generating property satisfying graphs by design: throughout the reverse process, we know that that the previous graph verified the property, so we can just check property satisfaction for the newly added edges (via incremental algorithm) that have not been checked yet (via edge blocking hashtable).

We compare the sampling runtimes of the aforementioned algorithmic variants in the table below. We run this experiment for the tree dataset, where we use acyclicity as target structural property. We picked this dataset due to its simpler incremental check, described in Appendix C.

Table 4: Runtimes comparison. We present the results for the methods we ran over five sampling runs in the format mean \pm standard error of the mean. For each run, we generated 100 graphs. All our experiments were run in individual Nvidia V100 32Gb GPUs. ConStruct [efficient] uses the edge blocking hashtable and the incremental version of the property satisfaction algorithm, while ConStruct [baseline] does not. DiGress+ refers to regular unconstrained generation, while DiGress+ [rejection] applies a *a posteriori* filtering of unconstrained generation until we get the intended amount of graphs.

Dataset	Sampling Time (s)
DiGress+	266.0 \pm 0.1
DiGress+ [rejection]	310.7 \pm 5.5
ConStruct [efficient]	290.2 \pm 0.1
ConStruct [baseline]	349.0 \pm 0.3

By implementing the edge blocking hashtable and the incremental checker, we observe a significant efficiency improvement: the additional runtime imposed by ConStruct over the unconstrained setting decreases from 31% to 9%. This trend should hold for other datasets as far as both lookup and update operations in hashtables ($O(1)$) and incremental property checks are more efficient than full-graph constraint checks, which is the typical case.

ConStruct also outperforms the *a posteriori* filtering of unconstrained generation. In this case, we used an unconstrained model that generates constraint satisfying properties 97% (DiGress+ in Table 1 of the paper), therefore largely benefitting the unconstrained model. For example, if we considered the digital pathology setting, where we can have only 6.6% (see Table 2 of paper, high TLS dataset, DiGress+) of the generated graphs with the unconstrained model satisfying the constraint, the amount of wasted computation would be dramatically larger, implying a much worse runtime. In such setting, ConStruct is approximately 12 times more efficient in generating valid graphs than DiGress+. Additionally, these gaps in efficiency may become particularly critical in settings where the amount of generated graphs is much larger, as is the case for molecular generation (2 orders of magnitude larger, see Appendix G).

E Synthetic Datasets

In this section, we provide further information about the unattributed synthetic datasets used in Section 4.1.

E.1 Statistics

In Table 5, we provide the minimum, maximum, and average number of nodes, minimum, maximum, and average number of edges, and the number of training, validation and test graphs used for each synthetic unattributed dataset.

Table 5: Synthetic dataset statistics. #Train, #Val and #Test denote the number of graphs considered in the train, validation and test splits, respectively

Dataset	Min. nodes	Max. nodes	Avg. nodes	Min. edges	Max. edges	Avg. edges	#Train	#Val	#Test
Planar	64	64	64	173	181	177.8	128	32	40
Tree	64	64	64	63	63	63	128	32	40
Lobster	11	99	50.2	10	99	49.2	64	16	20

E.2 Compared Methods

In Section 4, we compare ConStruct with several unconstrained graph generative models. We consider:

- the two first widely adopted autoregressive models for graph generation, GraphRNN [85] and GRAN [45];
- two spectrally conditioned methods: SPECTRE [53] is a GAN-based approach and HSpec-tre [6] consists of an iterative local expansion method that takes advantage of a score-based formulation;
- we also compare to the original implementation of DiGress [77] without the additional features described in Appendix A.1;
- GraphGen [23] is a scalable autoregressive method based on graph canonization through minimum DFS codes. Importantly, this method is domain-agnostic and supports attributed graphs by default;
- GraphGen-Redux [4] improves over GraphGen by jointly modelling the node and edge labels;
- BwR [16] and GEEL [33] also explore more scalable graph representations via bandwidth restriction schemes, which are then fed to other graph generation architectures;
- HDDT [32] leverages a K^2 -tree representation of graphs to capture their hierarchical structure in an autoregressive manner;
- GDSS [37] is a purely score-based formulation for graph generation;
- BiGG [13] is a parallelizable autoregressive model that takes advantage of graph sparsity to scale for large graphs;
- EDGE [9] is a degree-guided scalable discrete diffusion method (more details in Section 2);

F Digital Pathology

In this section, we go through additional information related to the digital pathology datasets.

F.1 Digital Pathology Primer

Digital pathology consists of an advanced form of pathology that involves digitizing tissue slides into whole-slide images (WSI), allowing for computer-based analysis and storage. Deep learning approaches quickly integrated digital pathology processing methods, primarily focusing on extracting image-level representations for tasks such as slide segmentation and structure detection. These have also been used for downstream tasks such as cancer grading, or survival prediction [5, 69]. However, existing image-based approaches face challenges with the size WSIs, requiring their patching. This procedure raises a trade-off between the context and the patch size provided to the model. Moreover, image-based deep learning lacks efficient representations of biological entities and their relations, resulting in less interpretable models. Recently, entity-graph based approaches have emerged as a promising alternative to evade such limitations [34, 2]. These graphs are built by directly assigning nodes to biological entities and modelling their interactions with edges [25, 34], providing enhanced predictive performance and interpretability [35, 80].

Importantly, most of the deep learning contributions in the digital pathology realm have been in the discriminative setting. However, digital pathology could profoundly benefit from the development of generative formulations in several dimensions: first, there is a lack of high-quality annotated samples, mostly due to their heavy ethical and privacy regulation. Besides, collecting these samples is remarkably costly both economically and in terms of time and labor required [34]. Most of the discriminative approaches are also instance-based. The developed models then become highly sensitive to distribution shifts, which is a common challenge across biomedical datasets, for instance due to batch effects [20]. The development of generative models in digital pathology can address these limitations by enabling both the generation of synthetic data and distribution-based characterisations of the data. Even though some approaches have been carried out using image-based methods (e.g., GANs [38] or even diffusion models [55]), these lack the advantages of graph-based approaches. To the best of our knowledge, graph-based generative modelling in digital pathology has only been explored by Madeira et al. [51]. Despite the promising results for data augmentation settings, only an off-the-shelf graph generative model (DiGress) is explored and in a proprietary dataset.

F.2 Building Whole-slide Cell Graphs

We build the whole-slide cell graphs from the genomic and clinical data available from the Molecular Taxonomy of Breast Cancer International Consortium (METABRIC) molecular dataset³. This dataset has been extensively used in previous breast cancer studies [65, 12, 14]. Using the single cell data, we mapped 32 different annotated cell phenotypes to 9 more generic phenotypes in a biologically grounded manner. We used the mapping detailed in Table 6. Therefore, each node is assigned to one of the resulting nine possible phenotypes. We assume these phenotypes to extensively characterize a cell both anatomically and physiologically.

Regarding edges, we followed the typical procedure for cell-graphs in digital pathology [34, 35, 2, 80]: first we used Delaunay triangulation on the cell positions to build them. Then, we discard edges longer than $25\ \mu m$. We note that we obtain different graphs than the ones considered by Danenberg et al. [14]. In terms of dimensionality, we obtain graphs with $b = 9$ and $c = 1$. We focus on the generation of simple yet biologically meaningful structures, Tertiary Lymphoid Structures (TLSs), further described in Appendix F.3. Thus, we extract 4-hop non-overlapping subgraphs centered at nodes whose class is "B-cell" from the whole-slide graphs.

F.3 Tertiary Lymphoid Structures

Tertiary Lymphoid Structures (TLSs) are simple yet biologically meaningful structures. Structurally, TLSs are well-organized biological entities where clusters of B-cells are enveloped by supporting T-cells. Typically observed in ectopic locations associated with chronic inflammation [60, 67], these structures have been linked to extended disease-free survival in cancer [27, 43, 17, 57, 67], thus

³Data retrieved from <https://zenodo.org/records/7324285>

Table 6: Mapping used to convert the original phenotypes to the adopted phenotypes.

Original Phenotype	Mapping Phenotype
CK8-18 ^{hi} CXCL12 ^{hi} HER2 ⁺ MHC ^{hi} CD15 ⁺ CK8-18 ^{hi} ER ^{lo} CK ^{lo} ER ^{lo} CK ^{lo} ER ^{med} CK8-18 ⁺ ER ^{hi} CK ^{med} ER ^{lo} MHC I & II ^{hi} Basal Ep CD57 ⁺ MHC I ^{hi} CD57 ⁺ ER ^{hi} CXCL12 ⁺ Ep Ki67 ⁺ CK ⁺ CXCL12 ⁺ CD15 ⁺	Epithelial
Endothelial	Endothelial
Macrophages & granulocytes Macrophages Granulocytes	Macrophages/Granulocytes
Fibroblasts Fibroblasts FSP1 ⁺	Fibroblast
Myofibroblasts Myofibroblasts PDPN ⁺	Myofibroblast
CD4 ⁺ T cells CD4 ⁺ T cells & APCs CD8 ⁺ T cells T _{Reg} & T _{Ex}	T
B cells	B
CD57 ⁺ Ki67 ⁺	Marker
CD38 ⁺ lymphocytes	CD38+ Lymphocyte

constituting an important indicator for medical prognosis in cancer. Since these are small structures when compared with the size of whole-slide graph, we extract non-overlapping 4-hop subgraphs centered at nodes whose class is “B-cell” from the WSI graphs. This procedure is illustrated in Figure 4.

As mentioned in Section 4.2, the TLS content of a cell graph can be quantified using the *TLS embedding*, $\kappa = [\kappa_0, \dots, \kappa_5] \in \mathbb{R}^6$ [67, 51]. This TLS-like organization metric considers only edges between B and T-cells and classifies them into several categories: α edges link two cells of the same type, while γ_j edges connect a B to a T-cell, where j is the number of B-cell neighbors of the B-cell vertex (see Figure 4). Therefore, the entry i of κ is defined as the proportion of its γ edges whose index is larger than i :

$$\kappa_i(G) = \frac{|E_{BT}| - |E_\alpha| - \sum_{j=0}^i |E_{\gamma_j}|}{|E_{BT}| - |E_\alpha|}, \quad (20)$$

where $|E_{BT}|$, $|E_\alpha|$, and $|E_{\gamma_j}|$ correspond to the number of edges between B and T-cells, of α edges and of γ_j edges in a given graph, G . By definition, note that the entries of κ take values between 0 and 1 and are monotonically non-increasing with i .

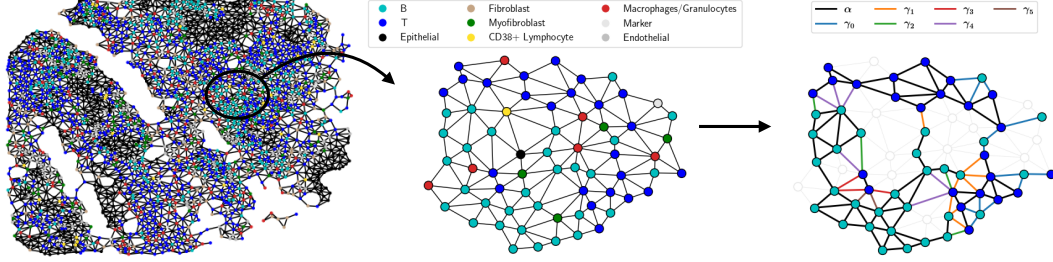


Figure 4: Extraction of a cell subgraph (center) from a WSI graph (left). From this cell subgraph, we can then compute the TLS embedding based on the classification of the edges into different categories, shown on the right. We can observe a cluster of B-cells surrounded by some support T-cells, characteristic of a high TLS content.

F.4 Statistics of digital pathology datasets

In this section we provide the statistics for the low and high TLS content datasets. In Table 7, we provide their structural statistics and, in Table 8, the prevalence for each of the nine phenotypes (after mapping) across all the nodes in the datasets. In Figure 5, we provide their entry-wise distributions for the TLS embedding, κ .

Table 7: Digital pathology datasets statistics. #Train, #Val and #Test denote the number of graphs considered in the train, validation and test splits, respectively.

Dataset	Min. nodes	Max. nodes	Avg. nodes	Min. edges	Max. edges	Avg. edges	#Train	#Val	#Test
High TLS	20	81	57.9	39	203	143.8	128	32	40
Low TLS	20	81	51.7	37	204	123.7	128	32	40

Table 8: Prevalence (in %) of the different cell phenotypes for the digital pathology datasets.

Dataset	B	CD38+ Lymphocyte	Endothelial	Epithelial	Fibroblast	Macrophages/Granulocytes	Marker	Myofibroblast	T
High TLS	39.3	1.9	4.6	9.4	4.4	6.3	0.6	7.2	26.4
Low TLS	7.7	2.4	5.9	33.4	17.7	8.4	0.2	9.9	14.1

F.5 Baseline Method for Digital Pathology

The non deep learning method used as baseline for the digital pathology dataset follows Madeira et al. [51]. This model learns three distributions by counting the proportions of given events in the train dataset. In particular:

- Categorical distribution for the number of nodes, where the probability of sampling a given number of nodes is the same as its proportion in the train dataset, D_{train} , i.e.:

$$P(|X| = k) = \frac{|\{G \in D_{\text{train}} : |X| = k\}|}{|D_{\text{train}}|},$$

- Categorical distribution for the cell phenotypes, where the probability for each cell phenotype corresponds to its marginal probability in the dataset:

$$P(\text{Ph}(\nu) = \text{ph}_i) = \frac{\sum_{G \in D_{\text{train}}} |\{\nu \in X : \text{Ph}(\nu) = \text{ph}_i\}|}{\sum_{G \in D_{\text{train}}} |X|},$$

where $\text{Ph}(\nu)$ refers to the phenotype of node ν , and ph_i denotes the specific phenotype labeled as i . These consist of the phenotypes described in Appendix F.2 with a fixed (arbitrary) order.

- Bernoulli distribution for the edge type (no edge vs edge) conditioned on the phenotypes of its two vertices, again computed based on its marginal distribution in the train set.

$$P(\text{Edge} \mid \text{Ph}(\nu_1) = \text{ph}_i, \text{Ph}(\nu_2) = \text{ph}_j) = \frac{\sum_{G \in D_{\text{train}}} |\{(v_1, v_2) \in C(G) : (v_1, v_2) \in E\}|}{\sum_{G \in D_{\text{train}}} |C(G)|},$$

where $C(G) = \{v_1 \in X : \text{Ph}(v_1) = \text{ph}_i\} \times \{v_2 \in X : \text{Ph}(v_2) = \text{ph}_j\}$ for $1 \leq \text{ph}_i < \text{ph}_j \leq 9$.

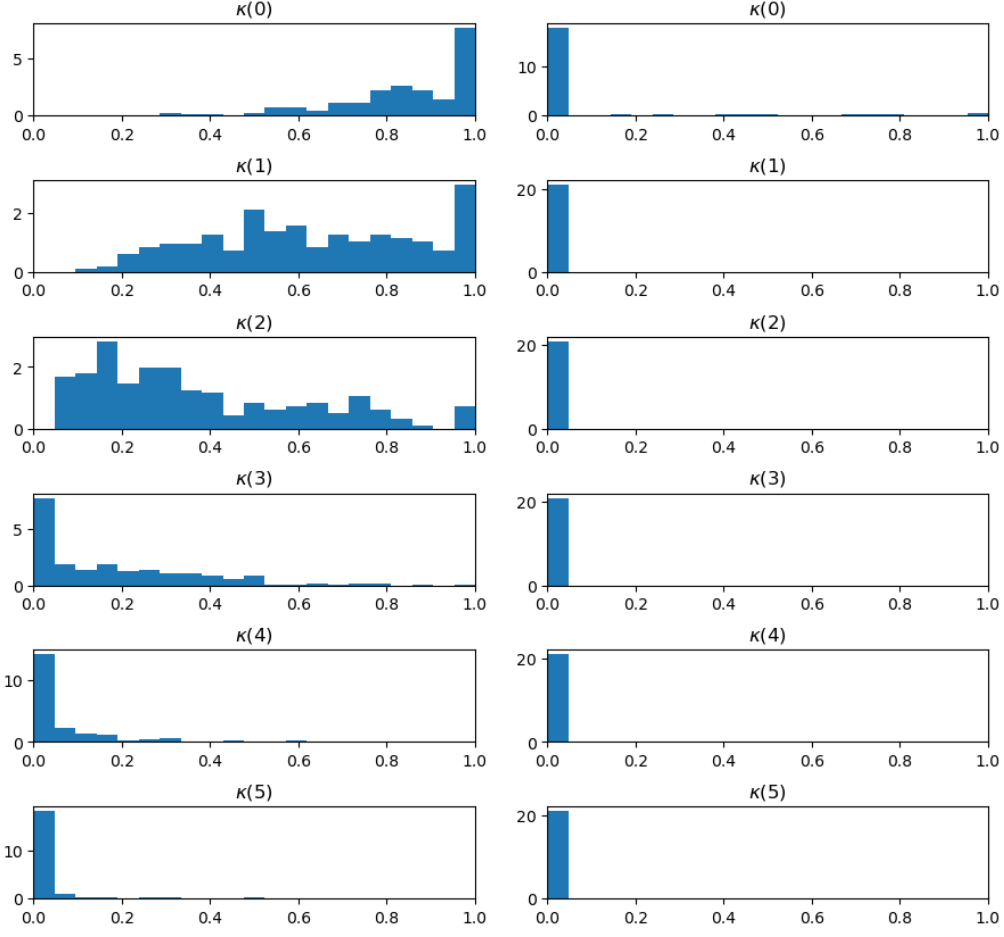


Figure 5: Distributions of the TLS embedding entries for high TLS (left) and the low TLS content (right) datasets.

To sample a new graph, we first sample a number of nodes for the graph from the first distribution. Then, for each of those nodes sample a cell phenotype from the second distribution. Finally, between every pair of cells, we sample an edge type given the two phenotypes previously sampled. This sampling algorithm is described in Algorithm 4.

Algorithm 4: Sampling Algorithm for the Digital Pathology Baseline

Input: Number of graphs to sample N

```

1 for  $i = 1$  to  $N$  do
2   Sample  $|X| \sim P(|X|)$ ;                                     // Number of nodes
3   for  $n = 1$  to  $|X|$  do
4      $X[n] \sim P(\text{Ph}(\nu))$ ;                                   // Sample node phenotypes
5   end
6   for  $1 \leq i < j \leq 9$  do
7      $E[i, j] \sim P(\text{Edge} \mid \text{Ph}(X[i]), \text{Ph}(X[j]))$ ;         // Sample edges
8   end
9   Store  $G = (X, E)$ ;
10 end

```

G Molecular Datasets

G.1 Exploring Planarity

In this section, we show the results for 3 molecular datasets: QM9 [79], MOSES [61] and GuacaMol [8]. Importantly, for QM9 and GuacaMol, we include formal charges as additional node labels, since this information has been shown beneficial for diffusion-based molecular generation [78]. For MOSES, such information is not available.

The metrics used to evaluate generation were:

- FCD - Fréchet ChemNet Distance [62], similar to Fréchet Inception Distance (FID) but for molecules, represented as SMILES. This metric evaluates sample quality in unconstrained settings.
- Uniqueness - proportion of not repeated molecules across all the generated molecules;
- Novelty - proportion of generated molecules that are not in the train set;
- Valid - proportion of valid molecules (checked using valencies). This metric evaluates sample validity.

In particular, we explore planarity as target structural property in the molecular setting, as previously suggested by recent works for the discriminative tasks [18]. Therefore, we also include the proportion of planar molecules from the generated set as an evaluation metric. As a remark, QM9 and MOSES are exclusively composed of planar molecules. GuacaMol contains 3 non-planar molecules out of 1273104 molecules in the train set and 3 non-planar molecules out of 238706 molecules in the test set. We considered these non-planar examples negligible in model training/evaluation, thus fully preserving the original dataset. The validation set has 79568 planar molecules. The results are shown in Table 9.

Table 9: Graph diffusion performance on molecular generation. The constraining property used for ConStruct is planarity. We present the results for the methods we ran over five sampling runs in the format mean \pm standard error of the mean. For each run, we generated 10000, 25000, and 18000 generated molecules for QM9, MOSES, and GuacaMol, respectively, following the protocol from Vignac et al. [77].

QM9 Dataset					
Model	FCD \downarrow	Unique \uparrow	Novel \uparrow	Valid \uparrow	Planarity \uparrow
Train set	1.0	100	0.0	100	100
DiGress+	0.2090 ± 0.0068	96.0 ± 0.1	36.6 ± 0.1	99.0 ± 0.0	99.7 ± 0.1
ConStruct	0.3443 ± 0.0061	96.1 ± 0.1	40.1 ± 0.2	98.5 ± 0.0	100.0 ± 0.0
MOSES Dataset					
Model	FCD \downarrow	Unique \uparrow	Novel \uparrow	Valid \uparrow	Planarity \uparrow
Train set	1.0	100	0.0	100	100
DiGress+	0.5447 ± 0.0080	100.0 ± 0.0	93.5 ± 0.1	87.5 ± 0.1	100.0 ± 0.0
ConStruct	0.6068 ± 0.0045	100.0 ± 0.0	93.7 ± 0.1	84.1 ± 0.1	100.0 ± 0.0
GuacaMol Dataset					
Model	FCD \downarrow	Unique \uparrow	Novel \uparrow	Valid \uparrow	Planarity \uparrow
Train set	1.0	100	0.0	100	≈ 100
DiGress+	0.9663 ± 0.0063	100.0 ± 0.0	100.0 ± 0.0	84.7 ± 0.2	99.9 ± 0.0
ConStruct	1.0538 ± 0.0045	100.0 ± 0.0	100.0 ± 0.0	81.9 ± 0.1	100.0 ± 0.0

We only observe an incremental improvement in the planarity satisfaction of the output graphs, since DiGress+ learns to almost always generate planar graphs. As a consequence, the constrained model ends up being marginally less expressive than the unconstrained model, as extensively discussed in Appendix H.1. This impacts both sample quality and sample validity. In fact, while for the

discriminative setting, the main aim is to design fully expressive architectures for classes of graphs as broad as possible, as demonstrated by PlanE [18] for planar graphs, for constrained generation, this is not the case. As exemplified in this case, planarity is too loose of a constraint, since the atoms composing molecules typically have low degrees and it becomes highly unlikely for the unconstrained diffusion model to violate planarity. This ends up slightly harming the performance of the constrained generative model without bringing the benefits of increased validity, as observed in Section 4.

As a side note for the interested reader, the low values of novelty for QM9 are a result of the nature of this dataset, which consists of an exhaustive enumeration of small molecules satisfying a given set of properties [76, 77]. Therefore, there is small room for the generation of new molecules within such domain.

G.2 Controlled Molecular Generation

In many real world scenarios, we want to generate molecules to target different goals, ranging from specific drug interactions to particular material properties. In such cases, we are not interested in generating any realistic molecules, but in obtaining molecules that are endowed with given properties matching our specific objectives. Constrained graph generation appears as a promising research direction to accomplish such tasks, as the generated molecules will necessarily verify the enforced properties by design. In this section, we explore how to use ConStruct to successfully address such challenge.

One relevant property of molecules is acyclicity. In molecules, this structural property dictates distinct chemical characteristics compared to their cyclic counterparts. In fact, acyclic molecules are frequently encountered in natural products and pharmaceuticals, where their linear structures contribute to enhanced solubility, bioavailability, and metabolic stability. Additionally, acyclic molecules offer simplified synthetic routes and reduced computational complexity in modeling studies.

In the Table below, we explore the generation of acyclic molecules by picking the absence of cycles as constraining property. Importantly, in contrast to all the experiments in the paper, we do *not* train with only graphs that verify the property. Instead, we use the two models trained in the unconstrained setting (from previous section): one with edge-absorbing transitions (ConStruct) and another with marginal transitions (Constrained DiGress+). We then sample from these models using the absorbing noise model and the projector for acyclicity. The results are presented in Table 10.

Table 10: Controlled graph diffusion for acyclic molecules. The constrained property used is the absence of cycles. Constrained DiGress+ denotes a model that was trained with a marginal noise model, but where the sampling is performed using the absorbing noise and projector. Both models were trained in the full QM9 dataset. We present the results for the methods we ran over five sampling runs in the format mean \pm standard error of the mean. For each run, we generated 10000 molecules, following the protocol from Vignac et al. [77].

Model	QM9 Dataset			
	Unique \uparrow	Novel \uparrow	Valid \uparrow	Acyclicity \uparrow
Train set	100	0.0	100	100
Constrained DiGress+	80.7 \pm 0.1	64.7 \pm 0.2	81.3 \pm 0.3	100.0 \pm 0.0
ConStruct	79.2 \pm 0.2	68.8 \pm 0.1	99.8 \pm 0.0	100.0 \pm 0.0

We observe that both methods output only acyclic molecules, which is a necessary consequence of the utilization of the projector. As the set of cyclic molecules is a subset of the set of unconstrained molecules, we verify some repetition among the generated samples. This leads to a decrease in the values of uniqueness for both models when compared to the unconstrained setting. Most remarkably, while the validity of the molecules generated by the model trained with the marginal noise model is significantly lower than the observed one for the unconstrained sampling setting, ConStruct preserves its high validity values (even higher than in the unconstrained setting). This result validates the foundation upon which ConStruct is laid: due to the marginal noise model, the forward process distribution does not match the reverse one when using the projector, harming the molecular validity of the generated instances. In contrast, the edge-absorbing noise model of ConStruct allows the forward and reverse processes to stay in distribution.

H Variants of ConStruct - Performance Analysis and Extensions

In this section, we perform some ablations to ConStruct/DiGress to further analyse its performance and explore methodological extensions to the proposed method.

H.1 Performance Analysis

From Table 1, we observed that, for the specific case of the tree dataset, DiGress+ outperforms ConStruct. To explain why, we start by noting that approximately 97% of the graphs generated by DiGress+ already comply with the target structural property. This value indicates that DiGress+ had access to sufficient data and it is sufficiently expressive to learn the dependencies of tree graphs almost perfectly, leaving little room for improvement with ConStruct. In contrast, for the lobster and planar datasets, the corresponding values of DiGress+ are significantly lower, hinting the pertinence of ConStruct in such scenarios.

However, this observation alone does not explain the slight performance gap. To investigate further, we ran DiGress+ with an edge-absorbing noise model but without projector, designating it as DiGress+ [absorbing] in Table 11. We observe a significant decrease in performance with this modification. This suggests that it is the choice of the noise model that is hindering ConStruct’s performance for this dataset. In fact, ConStruct outperforms DiGress+ [absorbing], emphasizing the relevance of the projector step. In any case, we remark that we did not adjust the variance schedule beyond the one proposed by Austin et al. [3], leaving room for potential improvement in this aspect. Nevertheless, we observe performance dataset dependency by applying the same modified model to the planar dataset (again, see table 11), where it exhibits a significantly better average ratio compared to DiGress+. This observation aligns with recent research indicating that there is no clear evidence that an optimal noise model can be deduced *a priori* from dataset statistics [75].

H.2 A Posteriori Modifications

An advantage of our setting is that the projector merely interferes with the sampling algorithm, avoiding to affect the efficiency of the diffusion model training. Otherwise, if we were to directly block the model’s predictions, it would require a constraint satisfaction check for each potentially added edge at every forward pass, resulting in a prohibitive computational overhead.

In contrast, we could also consider the opposite setting: only applying *a posteriori* modifications to graphs generated by the unconstrained model. Two possible alternatives emerge:

- **DiGress+ [rejection]** - we reject the final samples generated by the unconstrained model that do not satisfy the provided constraint. While we should expect a good performance from this approach, it wastes computational resources as it requires discarding the rejected graphs and restarting the whole sampling process until we get the desired amount of generated graphs.
- **DiGress+ [projection]** - we only apply the projector to the final samples generated by the unconstrained method. For example, in the case of the planarity as target property, we could find the maximal planar subgraphs of the generated samples. This method would necessarily provide a more efficient sampling procedure (as we only execute the projector step once).

We provide the results in synthetic graphs for both methods in Table 11. We observe that DiGress+ (rejection) attains great V.U.N. values, as expected. Nevertheless, we analyse its alarming computational inefficiencies in Appendix D.3. Additionally, we see that DiGress+ (projection) achieves worse performance than ConStruct. We attribute this result to the fact that such a scheme fails to inform the generative model about the constraining condition throughout the reverse process, thus not harnessing the full expressivity of the diffusion model. We also attribute the anomalously good performance of this method for the tree dataset to the optimal properties of the projector in such case (see Theorem 2).

Finally, considering the two extreme cases described above (blocking edges at every forward pass *vs a posteriori* modifications), we conclude that ConStruct finds itself in a sweet spot in the trade-off between additional computational burden and integration into the diffusion model.

H.3 Likelihood-based constrained generation

We also consider two variants of ConStruct where the projector is no longer independent from the diffusion model. Instead, we use the associated likelihoods to each of the sampled candidate edges at a given time step t , $p(e_{ij}^{t-1}|G^t)$, to define an order by which we add the edges. Therefore, instead of uniformly sampling them at random, we propose two methods of integrating such information:

- Deterministic: we add the edges with higher $p(e_{ij}^{t-1}|G^t)$ first.
- Stochastic: we sample without replacement from the set of candidates edges, where the probability of sampling each of them is proportional to the respective $p(e_{ij}^{t-1}|G^t)$.

We present the results for these likelihood-based variants of ConStruct in Table 11. As we can observe, for all the analysed datasets, the three ConStruct variants are statistically equivalent in terms of performance. In terms of efficiency, there is no meaningful difference among the three methods: even though the uniformly random sampling does not have to sort the order of the edges nor access the corresponding $p(e_{ij}^{t-1}|G^t)$, the computational overburden of these operations is negligible. We remark that the theoretical analysis performed in Appendix B also holds for the stochastic likelihood-based variant, but not for the deterministic one, as the latter is not able to select any permutation from the candidate edges with non-zero probability: up to the degenerate cases where different candidate edges have the same $p(e_{ij}^{t-1}|G^t)$, it always selects candidate edges by the same order.

Table 11: Graph generation performance on synthetic graphs. DiGress+, ConStruct are retrieved from Table 1, from which we follow the same experimental protocol. DiGress+ [absorbing] denotes DiGress+ with an edge-absorbing noise model. DiGress+ [rejection] refers to the baseline that rejects the unconstrainedly generated graphs that do not satisfy the constraint and resamples, while DiGress+ [projection] applies the projector on them. ConStruct [model - det] and ConStruct [model - stoch] denote the deterministic and stochastic likelihood-based variants of ConStruct.

Planar Dataset											
Model	Deg. ↓	Clus. ↓	Orbit ↓	Spec. ↓	Wavelet ↓	Ratio ↓	Valid ↑	Unique ↑	Novel ↑	V.U.N. ↑	Property ↑
Train set	0.0002	0.0310	0.0005	0.0038	0.0012	1.0	100	100	0.0	0.0	100
DiGress+	0.0008 ±0.0001	0.0410 ±0.0033	0.0048 ±0.0004	0.0056 ±0.0004	0.0020 ±0.0002	3.6 ±0.2	76.4 ±1.3	100.0 ±0.0	100.0 ±0.0	76.4 ±1.3	76.4 ±1.3
ConStruct	0.0003 ±0.0001	0.0403 ±0.0047	0.0004 ±0.0001	0.0053 ±0.0004	0.0009 ±0.0001	1.1 ±0.1	100.0 ±0.0	100.0 ±0.0	100.0 ±0.0	100.0 ±0.0	100.0 ±0.0
DiGress+ [absorbing]	0.0006 ±0.0002	0.0383 ±0.0041	0.0028 ±0.0005	0.0050 ±0.0002	0.0010 ±0.0001	2.4 ±0.2	42.4 ±1.0	100.0 ±0.0	100.0 ±0.0	42.4 ±1.0	42.4 ±1.0
DiGress+ [rejection]	0.0008 ±0.0001	0.0418 ±0.0035	0.0022 ±0.0001	0.0054 ±0.0004	0.0019 ±0.0001	2.6 ±0.2	100.0 ±0.0	100.0 ±0.0	100.0 ±0.0	100.0 ±0.0	100.0 ±0.0
DiGress+ [projection]	0.0003 ±0.0001	0.0347 ±0.0030	0.0013 ±0.0002	0.0056 ±0.0003	0.0015 ±0.0001	1.6 ±0.1	100.0 ±0.0	100.0 ±0.0	100.0 ±0.0	100.0 ±0.0	100.0 ±0.0
ConStruct [model - det]	0.0004 ±0.0001	0.0416 ±0.0040	0.0005 ±0.0002	0.0050 ±0.0003	0.0009 ±0.0001	1.3 ±0.2	100.0 ±0.0	100.0 ±0.0	100.0 ±0.0	100.0 ±0.0	100.0 ±0.0
ConStruct [model - stoch]	0.0004 ±0.0001	0.0404 ±0.0038	0.0005 ±0.0002	0.0050 ±0.0003	0.0009 ±0.0001	1.2 ±0.1	100.0 ±0.0	100.0 ±0.0	100.0 ±0.0	100.0 ±0.0	100.0 ±0.0
Tree Dataset											
Train set	0.0001	0.0000	0.0000	0.0075	0.0030	1.0	100	100	0.0	0.0	100
DiGress+	0.0002 ±0.0001	0.0000 ±0.0000	0.0000 ±0.0000	0.0092 ±0.0005	0.0032 ±0.0001	1.3 ±0.2	91.6 ±0.7	100.0 ±0.0	100.0 ±0.0	91.6 ±0.7	97.0 ±0.8
ConStruct	0.0003 ±0.0001	0.0000 ±0.0000	0.0000 ±0.0000	0.0073 ±0.0008	0.0034 ±0.0002	1.9 ±0.3	83.0 ±1.8	100.0 ±0.0	100.0 ±0.0	83.0 ±1.8	100.0 ±0.0
DiGress+ [absorbing]	0.0004 ±0.0002	0.0000 ±0.0000	0.0000 ±0.0000	0.0079 ±0.0006	0.0034 ±0.0002	2.3 ±0.5	72.8 ±0.6	100.0 ±0.0	100.0 ±0.0	72.8 ±0.6	85.6 ±1.4
DiGress+ [rejection]	0.0002 ±0.0001	0.0000 ±0.0000	0.0000 ±0.0000	0.0093 ±0.0004	0.0032 ±0.0000	1.4 ±0.3	100.0 ±0.0	100.0 ±0.0	100.0 ±0.0	100.0 ±0.0	100.0 ±0.0
DiGress+ [projection]	0.0002 ±0.0001	0.0000 ±0.0000	0.0000 ±0.0000	0.0092 ±0.0004	0.0031 ±0.0001	1.3 ±0.2	94.0 ±0.3	100.0 ±0.0	100.0 ±0.0	94.0 ±0.3	100.0 ±0.0
ConStruct [model - det]	0.0003 ±0.0001	0.0000 ±0.0000	0.0000 ±0.0000	0.0076 ±0.0008	0.0034 ±0.0001	1.9 ±0.3	83.2 ±1.7	100.0 ±0.0	100.0 ±0.0	83.2 ±1.7	100.0 ±0.0
ConStruct [model - stoch]	0.0004 ±0.0001	0.0000 ±0.0000	0.0000 ±0.0000	0.0072 ±0.0008	0.0034 ±0.0001	1.9 ±0.3	83.2 ±1.7	100.0 ±0.0	100.0 ±0.0	83.2 ±1.7	100.0 ±0.0
Lobster Dataset											
Train set	0.0002	0.0000	0.0000	0.0070	0.0070	1.0	100	100	0.0	0.0	100
DiGress+	0.0005 ±0.0001	0.0000 ±0.0000	0.0000 ±0.0000	0.0114 ±0.0006	0.0093 ±0.0005	1.8 ±0.1	79.0 ±1.1	98.0 ±0.7	96.6 ±0.6	69.4 ±1.2	76.8 ±1.7
ConStruct	0.0003 ±0.0001	0.0000 ±0.0000	0.0000 ±0.0000	0.0092 ±0.0009	0.0074 ±0.0004	1.3 ±0.2	86.8 ±2.4	98.8 ±0.6	97.0 ±0.9	83.2 ±2.3	100.0 ±0.0
DiGress+ [rejection]	0.0006 ±0.0001	0.0000 ±0.0000	0.0000 ±0.0000	0.0130 ±0.0010	0.0106 ±0.0006	2.1 ±0.2	100.0 ±0.0	96.4 ±0.2	95.6 ±0.8	93.6 ±0.8	100.0 ±0.0
DiGress+ [projection]	0.0006 ±0.0001	0.0000 ±0.0000	0.0000 ±0.0000	0.0109 ±0.0006	0.0098 ±0.0005	2.0 ±0.1	77.8 ±1.2	98.2 ±0.6	96.6 ±0.6	73.6 ±1.0	100.0 ±0.0
ConStruct [model - det]	0.0003 ±0.0001	0.0000 ±0.0000	0.0000 ±0.0000	0.0093 ±0.0008	0.0075 ±0.0003	1.2 ±0.1	87.0 ±2.3	98.8 ±0.6	97.0 ±0.9	83.4 ±2.2	100.0 ±0.0
ConStruct [model - stoch]	0.0003 ±0.0001	0.0000 ±0.0000	0.0000 ±0.0000	0.0093 ±0.0008	0.0075 ±0.0003	1.2 ±0.1	87.0 ±2.3	98.8 ±0.6	97.0 ±0.9	83.4 ±2.2	100.0 ±0.0

I Visualizations

In this section, we provide several visualizations of the final generated graphs, comparing them to the ones observed in the different datasets. We also visually expose the effect of the projector in different timesteps.

I.1 Graphs generated by ConStruct

Here we visually compare the graphs from the different datasets to the ones generated by ConStruct.

I.1.1 Synthetic Datasets

We provide plots of the sampled graphs from ConStruct for the different datasets: planar in Figure 6, tree in Figure 7, and lobster in Figure 8.

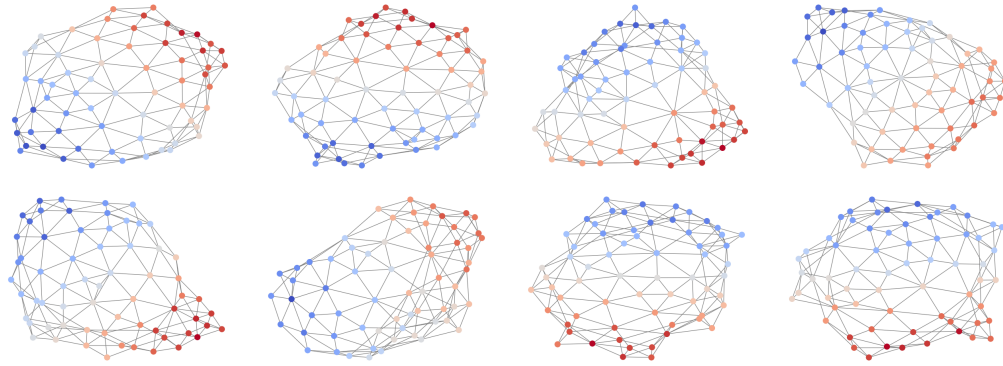


Figure 6: Uncurated set of dataset graphs (top) and generated graphs by ConStruct (bottom) for the planar dataset.

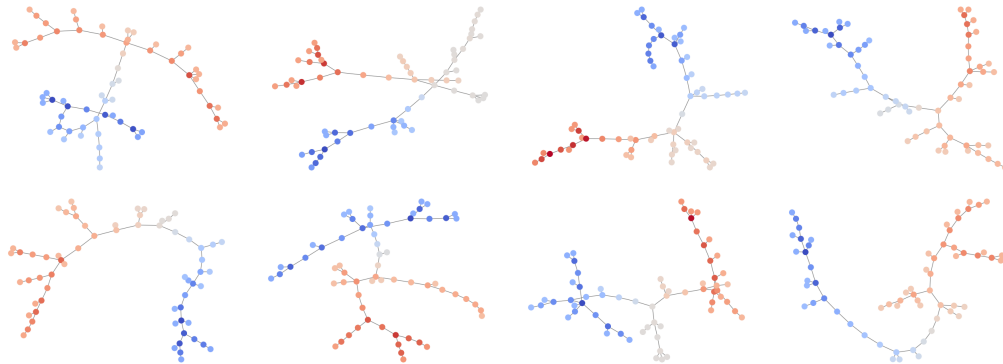


Figure 7: Uncurated set of dataset graphs (top) and generated graphs by ConStruct (bottom) for the tree dataset.

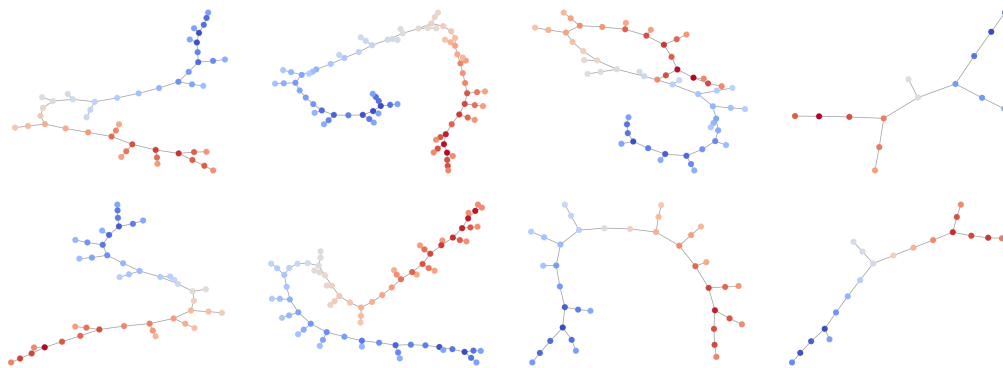


Figure 8: Uncurated set of dataset graphs (top) and generated graphs by ConStruct (bottom) for the lobster dataset.

1.1.2 Digital Pathology

We provide plots of the sampled graphs from ConStruct for the low TLS content dataset in Figure 9 and for the high TLS content dataset in Figure 10. We also several snapshots throughout the reverse process of ConStruct in Figure 11 to illustrate it as an edge insertion procedure.

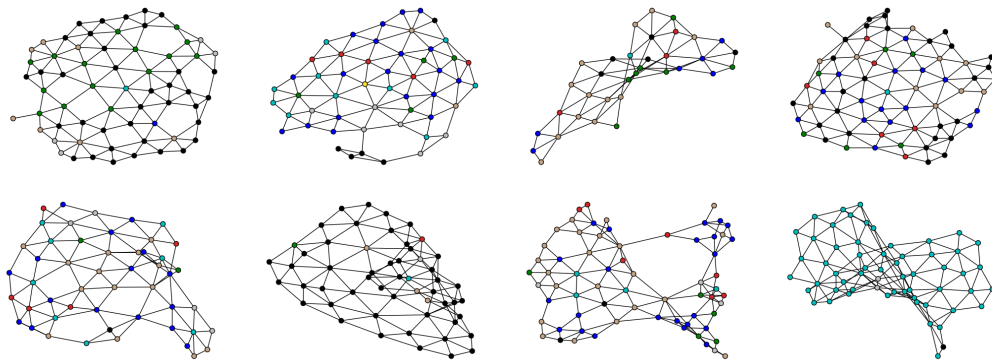


Figure 9: Uncurated set of dataset graphs (top) and generated graphs by ConStruct (bottom) for the low TLS dataset. The phenotype color key is presented in Figure 4.

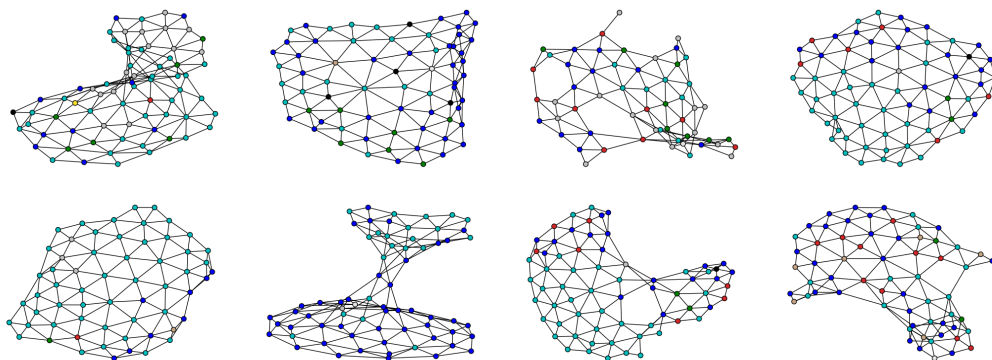


Figure 10: Uncurated set of dataset graphs (top) and generated graphs by ConStruct (bottom) for the high TLS dataset. The phenotype color key is presented in Figure 4.

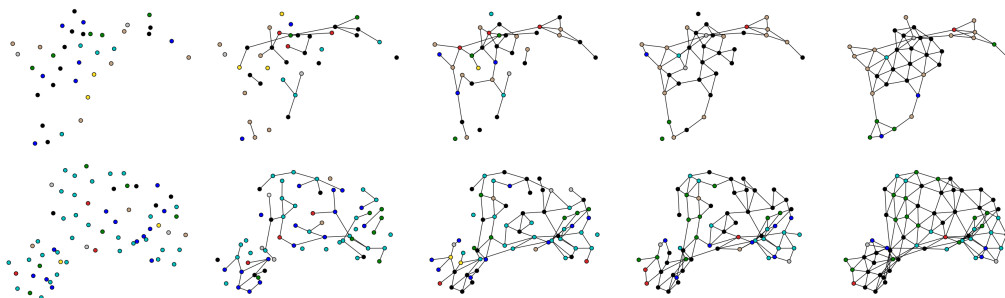


Figure 11: Reverse processes for generation of low (top) and high (bottom) TLS content graphs using ConStruct. We start from a graph without any edge on the left ($t = T$) and progressively construct the graph, as a consequence of the absorbing noise model. The node types switch due to the marginal noise model. On the right, we have a fresh new sample ($t = 0$). The phenotypes color key is presented in Figure 4.

I.2 Visualizing Intermediate Graphs (Before and After Projector)

In this section, we provide some visualizations of intermediate graphs obtained throughout the reverse process for three different datasets: planar, tree, and lobster. In Figure 12, we highlight the effect of the projector in rejecting the candidate edges that lead to property violation.

J Impact Statement

The primary objective of this paper is to enhance graph generation methodologies by enabling the integration of hard constraints into graph diffusion models. Although this problem holds significance for several real-world applications, including digital pathology and molecular generation, as exemplified in the paper, as well as protein design, the potential implications extend to advances in biomedical and chemical research. This development has the capacity to yield both positive and negative societal outcomes. Nonetheless, despite the potential for real-world impact, we currently do not identify any immediate societal concerns associated with the proposed methodology.

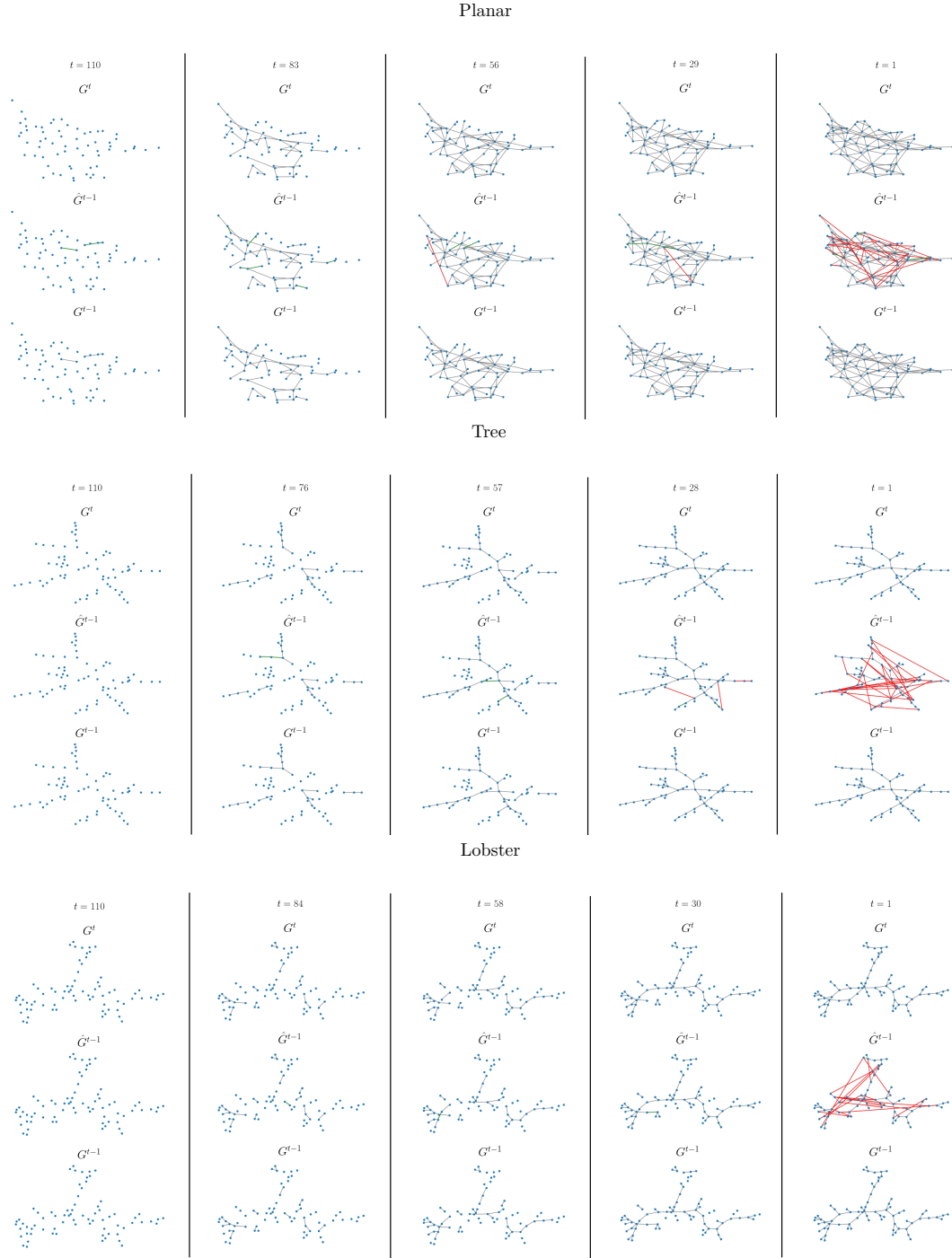


Figure 12: Visualizations of intermediate graphs throughout the reverse process. The notation follows the one of the rest of the paper: we obtain G^{t-1} after projecting \hat{G}^{t-1} , which in turn is obtained from G^t through the diffusion model. From the new edges obtained in \hat{G}^{t-1} , we color them in green when they do not break the constraining property and in red otherwise. We can observe that the red edges are rejected. To better emphasize the edge rejection by the projector, we do not use a fully trained model and use a trajectory length, T , smaller than usual.